Theses and Dissertations

Theses, Dissertations, and Senior Projects

January 2015

Hydrogen Adsorption Into Covalent Organic Frameworks

Aaron Koenig

Follow this and additional works at: https://commons.und.edu/theses

HYDROGEN ADSORPTION INTO COVALENT ORGANIC FRAMEWORKS

by

Aaron Robert Virgil Koenig
Bachelor of Arts, Saint John's University, 2012

A Thesis

Submitted to the Graduate Faculty

of the

University of North Dakota

in partial fulfillment of the requirements

for the degree of

Master of Science

Grand Forks, North Dakota
May
2015

This thesis, submitted by Aaron Koenig in partial fulfillment of the requirements for the Degree of Master of Science from the University of North Dakota, has been read by the Faculty Advisory Committee under whom the work has been done and is hereby approved.

_____
Dr. Jerome Delhommelle, Chairperson

_____
Dr. Evguenii Kozliak

_____
Dr. Kathryn Thomasson

This thesis is being submitted by the appointed advisory committee as having met all of the requirements of the School of Graduate Studies at the University of North Dakota and is hereby approved

_____
Wayne Swisher
Dean of the School of Graduate Studies

_____
april 29, 2015
Date

iii

PERMISSION

Title	Hydrogen Adsorption into Covalent Organic Frameworks
Department	Chemistry
Degree	Master of Science

In presenting this thesis in partial fulfillment of the requirements for a graduate degree from the University of North Dakota, I agree that the library of this University shall make it freely available for inspection. I further agree that permission for extensive copying for scholarly purposes may be granted by the professor who supervised my thesis work or, in his absence, by the Chairperson of the department or the dean of the School of Graduate Studies. It is understood that any copying or publication or other use of this thesis or part thereof for financial gain shall not be allowed without my written permission. It is also understood that due recognition shall be given to me and to the University of North Dakota in any scholarly use which may be made of any material in my thesis.

Aaron Koenig
April 27, 2015

TABLE OF CONTENTS

LIST OF FIGURES

LIST OF TABLES

ACKNOWLEDGMENTS

I wish to first acknowledge Prof. Jerome Delhommelle for bringing me to the University of North Dakota and serving as my advisor. I would also like to thank my committee members, Prof. Kathryn Thomasson and Prof. Evguenii Kozliak for contributions of their time and knowledge so that I may succeed. Also, many thanks to my fellow research group members: Dr. Caroline Desgranges, Dr. Tsvetan Aleksandrov, Dr. Kenneth Ndumbe Ngale, Jason Hicks, Erica Hicks, and Andrew Owen.

I wish to express my gratitude to the rest of the UND Chemistry Department's faculty and staff for their help and for providing a wonderful environment to work in. Also special thanks to Dr. Gautham Krishnamorthy of the UND Chemical Engineering Department for allowing me into two of his classes, both of which I thoroughly enjoyed. Last but not least, I acknowledge my friends and family for their constant support throughout my life.

To my fantastic parents, John and Karla.

ABSTRACT

The practicality of hydrogen power vehicles relies on the existence of an effective onboard storage method. Using expanded Wang-Landau simulations, we study the adsorption of hydrogen in a series of covalent organic frameworks (COF-102, COF-105 and COF-108). From which adsorption isotherms of H_2 are generated at temperatures of 77 K and 298 K. At 77 K the COFs are on par with the Department of Energy's 2015 targets, but fall short at 298 K. Molecular dynamic simulations of hydrogen in the COFs were also performed. From which the mean square displacement of the H_2 molecules was measured to obtain the diffusion coefficients of H_2 inside the COFs. As to be expected, the diffusion coefficients were found to be lower than bulk H_2 and possessed a relative order that corresponds with the pore sizes of the COFs.

CHAPTER 1

INTRODUCTION

The development of alternatives to petroleum fuel sources is a quickly growing trend in today's society. One such area that has seen rigorous study is that of hydrogen powered vehicles. Vehicles that are capable of being powered by H_2 have been created, but a major technical shortcoming is the lack of a safe, practical, and economical onboard hydrogen storage system. Storage via conventional compressed H_2 does not only possess safety concerns but it also falls short in storage efficiency. Liquid hydrogen storage systems perform better, but still do not provide a sufficient storage method as the gains in hydrogen capacity is negated by the additional costs of liquid H_2 storage. Another approach is by H_2 adsorption into highly porous carbon based materials. This approach has gained significant attention after the introduction of a relatively new material called metal organic frameworks (MOFs). MOFs are porous crystalline structures composed of metal ions linked together by organic molecules and have displayed promising H_2 storage capacities. In an effort to create a material with a lower density, the metal centers were removed and the resulting material was termed as covalent organic frameworks (COFs). Like MOFs, COFs are porous crystalline solids but are instead made from light elements (H, B, C, N, O, and Si) which are linked by strong covalent bonds. COFs were first synthesized Côté *et al.* 2005 [1] and were found to have high surface areas, pore volumes, thermal stabilities exceeding 500 °C and also very low densities. In fact COF-108 is reported to have

the lowest density of all known crystalline materials (0.17 g cm^{-3}) [2]. Given these characteristics, much research has been done towards the development of COFs and their hydrogen adsorption abilities.

1.1   Applications

The various potential practical applications has provided much motivation towards the increased study of COFs. These applications include: heterogeneous catalysis, semiconduction, and photoconduction [9–11]. However, the prominent feature of COFs are their high surface areas and pore volumes which results in excellent adsorptive properties. Their adsorption and storage abilities of gases such as, hydrogen, methane, and carbon dioxide have drawn much attention. The ability of COFs to separate gaseous mixtures has also been suggested, particularly the separation of hydrogen and methane, but it is still relatively undeveloped [12].

The most studied application by far is the ability of COFs to serve as hydrogen storage materials. The development of alternatives to gasoline powered vehicles has resulted in many promising prospects, one such being hydrogen powered vehicles. Hydrogen serves as an excellent alternative to gasoline because it has a high power density, is readily available, and exhibits a clean non-polluting combustion. Hydrogen powered vehicles have already been developed, but their economic feasibility is greatly hindered by a great lack of efficient onboard hydrogen storage systems. Research of the required performance of H_2 storage systems has been performed and from which the Department of Energy (DOE) has set goals for the year 2010 and 2015 as well as the ultimate goals that outline the specifications needed for practical use of hydrogen powered vehicles (Table 1.1) [13].

It should be kept in mind that the values in Table 1.1 are of deliverable H_2 and the weight and volume of the entire storage system is to be included in capacity

2

Table 1.1. DOE Storage System Targets for Light-Duty Vehicles [13]

Target	2010	2015	Ultimate
System Gravimetric Density (% wt)	4.5	5.5	7.5
System Volumetric Density (g L^{-1})	28	40	70

Quantities represent deliverable H_2 at ambient temperatures and pressure not exceeding 100 bar

calculations. Currently hydrogen is primarily stored in high-pressure tanks and also in liquid form, but both of these methods do not provide efficient storage and also give rise to safety concerns. Storage of hydrogen by adsorption into other porous materials has provided promising results, therefore H_2 adsorption in COFs has drawn great interest.

Both of these types can be expressed in either gravimetric or volumetric units. The calculation of either excess or total uptake in gravimetric units is shown in Equation 1.1.1 [14].

$$H_2 \ wt\% = \left(\frac{mass \ H_2}{mass \ sample + mass \ H_2} \right) \times 100\% \qquad (1.1.1)$$

Both the gravimetric and volumetric uptake are important when considered for practical applications, as both the weight and the volume of the system must be considered.

CHAPTER 2

COVALENT ORGANIC FRAMEWORKS

COFs are synthesized through the use of the relatively new concept of reticular chemistry. Reticular chemistry is the linking of what are referred to as secondary building units (SBUs) through strong covalent bonds into predetermined structures [3]. Reversible reactions under thermodynamic control are used to allow for an effective crystallization process that limits the amount of defects present in the framework. The use of reversible reactions allow for the thermodynamic product to form eventually if not initially and results in the formation of a very stable and highly crystalline product. The synthetic method, conditions, and the SBUs must be carefully chosen to allow for the thermodynamic control in the synthesis of COFs. Specifically, the SBU must contain groups capable of the formation of a connection between them through a reversible reaction and must also be conformationally rigid. Examples of SBUs are presented in Figures 2.1 and 2.2.

The first COF was reported in A. P. Côté et al. 2005 [1] in which the synthesis of both COF-1 and COF-5 was described. They used boronic acids as SBUs which are able to be joined together through condensation reactions to form boroxaine. COF-1 was formed through the self-condensation of 1,4-benzenediboronic acid (BDBA) (Figure 2.1a). The reaction was carried out in a flame sealed Pyrex tube with an internal pressure of 150 mTorr. After the tube was sealed, it was heated at 120 °C for 72 hours to yield the white product. It was found that an internal

pressure of 150 mTorr provided the highest yields and best crystalline structure. Higher pressures did not allow for the volatilization of H_2O from the reaction mixture therefore more starting material was present, whereas lower pressures resulted in more amorphous products because less gaseous H_2O was able to reenter the reaction mixture to break the undesired bonds. COF-5 was formed through the condensation of BDBA and 2,3,6,7,10,11-hexahydroxytriphenylene (HHTP) (Figure 2.1b) and followed the same procedure used for the synthesis of COF-1. Another type of 2D-COF is linked through hydrazine bonds and was also synthesized with a nearly identical procedure where condensation of 2,5-diethoxyterephthalohydrazide (Figure 2.1c) with 1,3,5-triformylbenzene or 1,3,5-tris(4-formylphenyl)benzene (Figure 2.1d,e) forms COF-42 and COF-43 respectively [4].

Most 2D-COFs form hexagonal planar sheets similar to graphite. These sheets also form layers with two possible stacking patterns, eclipsed (AA stacking) or slipped (AB stacking). Simulated powder X-ray diffraction (PXRD) was used to determined that the favored stacking pattern for COF-1 was staggered and all other COFs studied (COF-5, COF-6, COF-8, COF-10) preferred eclipsed stacking [1, 5]. Important properties of absorbent materials such as surface areas and pore volumes of the COFs was also determined and is shown in Table 2.1 [2, 4–8].

A similar procedure was used to synthesize the first 3D-COFs in 2007 as described in El-Kaderi *et al.* [2]. The difficulty in the synthesis of 3D-COFs is that the amount of different structures is essentially limitless, thus the synthesis relies on the predetermination of the most stable configuration. They determined the net types of **ctn** and **bor** topology to be the preferred configurations when the proposed SBUs were used. With this information the synthesis of 3D-COFs was designed as follows. COF-102 and COF-103 were formed through the self-condensation of tetra(4-dihydroxyborylphenyl)methane (TBPM) and tetra(4-dihydroxyborylphenyl)silane (TBPS) (Figure 2.2a,b) respectively. The co-condensation of TBPM or TBPS with
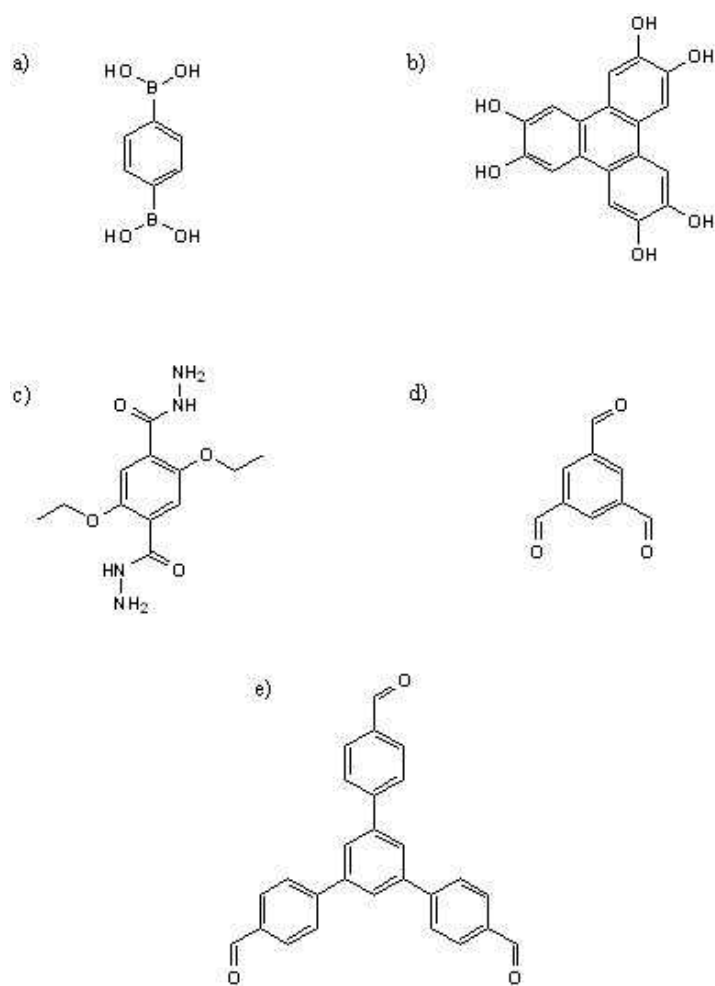
Figure 2.1. Two-dimensional secondary building units.

HHTP (Figure 2.1b) yielded COF-105 and COF-108 respectively. The reaction was also carried out in a sealed Pyrex tube with an internal pressure of 150 mTorr and was heated at 85 °C for 4 days. The densities of these four COFs are very low: COF-102 (0.41 g cm^{-3}), COF-103 (0.38 g cm^{-3}), COF-105 (0.18 g cm^{-3}), and COF-108 (0.17 g cm^{-3}) with COF-108 having the lowest density of all known crystalline materials. A different class of 3D-COFs which are constructed through very strong borosilicate bonds have also been synthesized in a similar way by the condensation of tetra(4-dihydroxyborylphenyl)methane with *tert*-butylsilane triol (Figure 2.2a,c) to yield COF-202 [6]. Also, imine linked COFs have been synthesized with the same procedure. COF-300 is formed from the condensation of tetra-(4-anilyl)-methane with linear terephthaldehyde (Figure 2.2d,e) [7]. The structures of the of all the COFs were determined with PXRD and were found to match the predetermined structures. The surface areas and pore volumes of these 3D-COFs was also ascertained and are displayed in Table 2.1 [2, 4–8].

Table 2.1. Surface Areas and Pore Volumes of 2D and 3D COFs [2, 4–8]

	Surface Area (m^2g^{-1})	Pore Volume (cm^3g^{-1})
COF-1	711	0.32
COF-5	1590	1.00
COF-6	980	0.32
COF-8	1400	0.69
COF-10	2080	1.44
COF-42	710	0.31
COF-43	620	0.36
COF-102	3472	1.32
COF-103	4210	1.66
COF-105	6502.61*	5.05*
COF-108	6277.99*	5.26*
COF-202	2690	1.09
COF-300	1360	0.72

*Indicates theoretical values
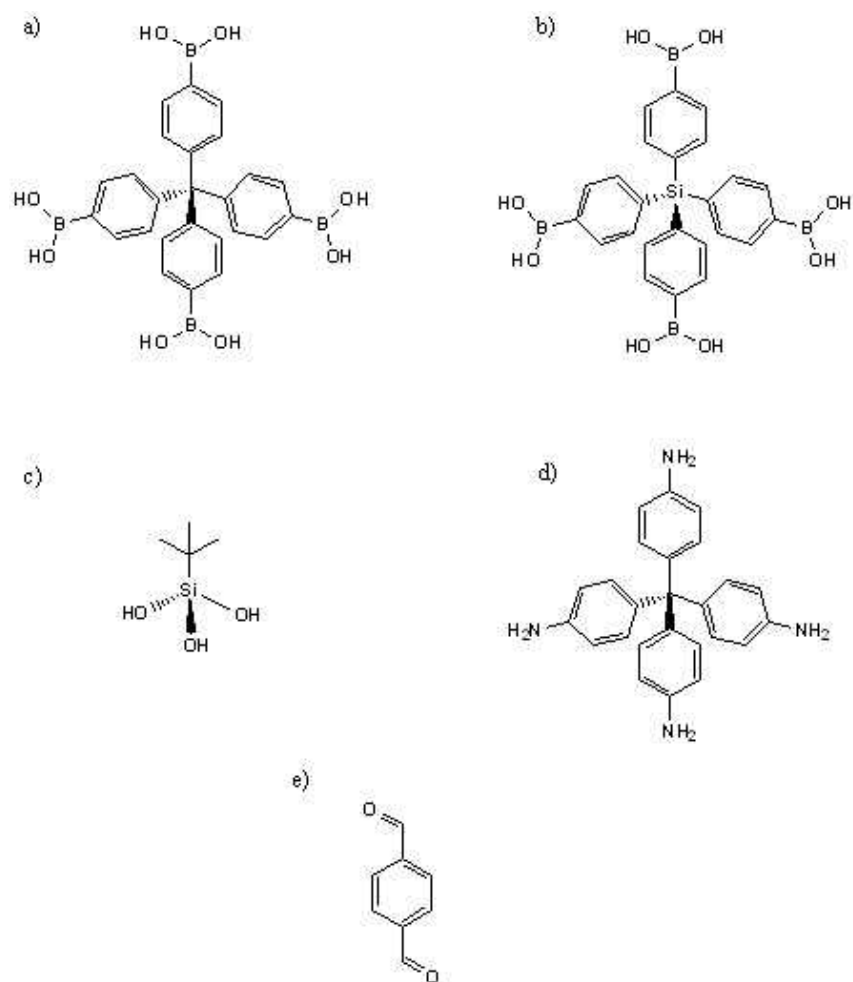
Figure 2.2. Three-dimensional secondary building units.

CHAPTER 3

ADSORPTION CONCEPTS

The adhesion of ions, atoms, or molecules of a gas, liquid, or dissolved solid, termed the adsorbates, to a surface, termed the adsorbent, is defined as adsorption. This process differs from that of absorption, which describes the process of a substance being taken up by a volume rather than a surface. A common example of such a process occurs when a liquid absorbs a gas (water absorbing oxygen). The term sorption can be used to describe both phenomena. In literature, and this thesis, the term adsorption is used to describe the case of hydrogen's interaction with COFs. One could argue that in the case of COFs, a volume is absorbing H_2 molecules. However, it is accurate to use adsorption as opposed to absorption since hydrogen is not really penetrating the COF, but rather moving through the pores and sticking to the interior surfaces.

Adsorption can be described as either physisorption or chemisorption. Chemisorption results from orbital interactions in which the adsorbate forms a chemical bond with the adsorbent. Hydrogen storage by means of chemisorption has been investigated with metal hydrides. However they have yet to be deemed a feasible storage technique since they have low gravimetric uptake and also exhibit poor H_2 delivery due to the stronger interaction of chemisorption. Physisorption on the other hand is bound through van der Waals and electrostatic forces. In the case of hydrogen, electrostatic forces have little role in adsorption as H_2 is a neutral molecule without a

dipole moment, therefore van der Waals interactions are the dominant forces present.

3.1 Models

Adsorption is an exothermic spontaneous process that is not entropically favored, thus adsorbents will hold more adsorbates at low temperature and high pressure. Adsorption measurements of the amount adsorbed are performed at various temperatures and pressures and data is most commonly displayed as isotherms. The shape of these isotherms are dependent on the nature of both the adsorbate and adsorbent and can generally be classified as one of five types, which are shown in Figure 3.1 [15].

Efforts of deriving mathematical adsorption models predate the classification of adsorption isotherms, one of the more notable being the work of Irving Langmuir. In a 1915 journal article investigating the formation of oxide layers on tungsten filament of light bulbs[16] he proposed a model which he later developed into the Langmuir equation shown below as

$$\theta = \frac{\alpha P}{1 + \alpha P}. \tag{3.1.1}$$

Where θ is the fractional coverage of the surface by the adsorbate, P is the gas pressure and α a constant. This equation models monolayer adsorption which corresponds to a type I isotherm in Figure 3.1.

The rest of the isotherm types are a result of the formation of multiple layers of adsorbates. The low pressure region of the type II is of the same shape as type I isotherm indicating the formation of a monolayer but it continues with a growth of a multilayer. Type III isotherms show that monolayer formation does not occur, rather growth of a multilayer starts immediately. Types IV and V correspond to types II and III respectively with the difference being that the isotherms plateau before the

10
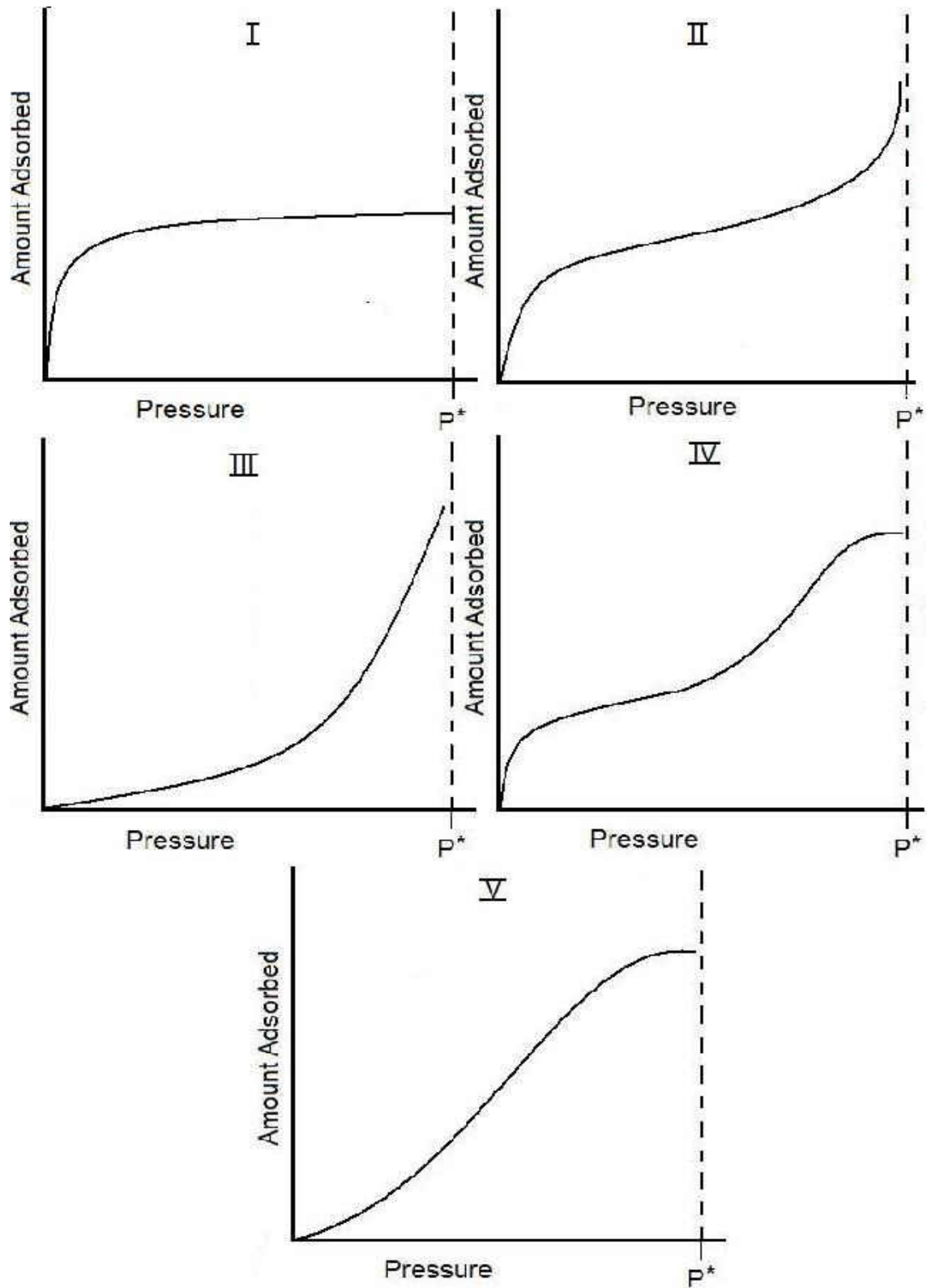
Figure 3.1. Isotherm types labeled I -V. Where P* is the saturation vapor pressure [15].

saturation pressure as a result of capillary condensation.

The first successful derivation of an adsorption model that included multilayer formation was the BET equation named from its creators: Brunauer, Emmett and Teller [17]. Their formulation of the BET equation starts with the assumption that each first layer constituent serves as one adsorption site for the next layer and so on. Next, s_0, s_1, s_2, ... s_i are defined as the area covered by the 0, 1, 2 ... i layers of adsorbates respectively. Therefore the total area of the solid, A, is given by Equation 3.1.2 and if we define v_0 as the volume adsorbed per area of a completely filled monolayer then the volume of the adsorbate v is given by Equation 3.1.3.

$$A = \sum_{i=0}^{\infty} s_i \tag{3.1.2}$$

$$v = v_0 \sum_{i=0}^{\infty} i s_i \tag{3.1.3}$$

Dividing the volume adsorbed over the total surface area of the adsorbent gives

$$\frac{v}{A v_0} = \frac{v}{v_m} = \frac{\sum_{i=0}^{\infty} i s_i}{\sum_{i=0}^{\infty} s_i} \tag{3.1.4}$$

where v_m is the volume adsorbed of a completely filled monolayer. This equation will be of use later in the derivation.

At equilibrium the rate of condensation on the zero layer (clean adsorbent) is equal to the evaporation of the first layer expressed as

$$a_1 p s_0 = b_1 s_1 \exp(-E_1/RT) \tag{3.1.5}$$

where p is the pressure, E_1 is the heat of adsorption of the first layer, and a_1 and b_1 are constants. Similarly the relation between the first and second adsorbate layers is given by

$$a_2 p s_1 = b_2 s_2 \exp(-E_2/RT) \tag{3.1.6}$$

and so on

$$a_i p s_{i-1} = b_i s_i \exp(-E_i/RT). \tag{3.1.7}$$

The pivotal assumption to simplify the BET equation is to assume the evaporation–condensation properties of the adsorbate in the second and higher layers to be equal to those of the bulk fluid such that

$$E_2 = E_3 \ldots = E_i = E_L \tag{3.1.8}$$

where E_L is the heat of liquefaction of the bulk fluid, and

$$\frac{b_2}{a_2} = \frac{b_3}{a_3} \ldots = \frac{b_i}{a_i}. \tag{3.1.9}$$

With these assumptions and rewriting Equation 3.1.5 to

$$
\begin{aligned}
s_1 &= y s_0 \\
y &= \frac{a_1}{b_1} p \exp(E_1/RT)
\end{aligned}
\tag{3.1.10}
$$

and Equation 3.1.6 to

$$
\begin{aligned}
s_2 &= x s_1 \\
x &= \frac{a_2}{b_2} p \exp(E_L/RT)
\end{aligned}
\tag{3.1.11}
$$

or in general

$$s_i = x s_{i-1} = x^{i-1} s_1 = y x^{i-1} s_0 = c x^i s_0 \tag{3.1.12}$$

13

where

$$c = \frac{y}{x} = \frac{a_1 b_2}{a_2 b_1} \exp((E_1 - E_L)/RT), \tag{3.1.13}$$

allows for the substitution of Equation 3.1.12 into Equation 3.1.4 to yield

$$\frac{v}{v_m} = \frac{cs_0 \sum_{i=1}^{\infty} ix^i}{s_0[1 + c\sum_{i=1}^{\infty} x^i]}. \tag{3.1.14}$$

The geometric series of the denominator and the numerator can be expressed as Equations 3.1.15 and 3.1.16 respectively. Note that if the number of possible layers was restricted to one, then Equation 3.1.14 reduces to the Langmuir equation. (Equation 3.1.1)

$$\sum_{i=1}^{\infty} x^i = \frac{x}{1 - x} \tag{3.1.15}$$

$$\sum_{i=1}^{\infty} ix^i = \frac{x}{(1 - x)^2} \tag{3.1.16}$$

Inserting them into Equation 3.1.14 and simplifying gives

$$\frac{v}{v_m} = \frac{cx}{(1 - x)(1 - x + cx)}. \tag{3.1.17}$$

The amount adsorbed on a free surface at saturation pressure p_0 is is infinite therefore to scale Equation 3.1.17, $x = p/p_0$. Inputing this new definition for x into Equation 3.1.17 and simplifying yields the BET equation shown below as

$$v = \frac{v_m cp}{(p_0 - p)[1 + (c - 1)p/p_0]}. \tag{3.1.18}$$

This can be transformed to

$$\frac{p}{v(p_0 - p)} = \frac{1}{v_m c} + \frac{c-1}{v_m c} \frac{p}{p_0}, \qquad (3.1.19)$$

which allows for the plot of $p/[v(p_0$ - $p)]$ over p/p_0 to give a line with slope $(c\text{-}1)/(v_m c)$ and an intercept of $1/(v_m c)$. This form of the BET equation is applicable to adsorption types II and III. For type II isotherms, c is greater than 2. When c is positive and less than 2, the shape is of a type III isotherm [18]. Equations for use with type IV and V isotherms were derived in the same way as above with the difference being that adjustments to the number of possible layers and the energy of the layer in the capillaries are made [15].

The principle application of the BET equation is the determination of the surface area of porous solids [19]. This is performed by generating an adsorption isotherm with the solid adsorbent and a gas such as nitrogen as the adsorbate. In the case of type II or III the isotherm is fitted to Equation 3.1.19 to determine v_m, which for simplicity in specific surface area determination we will express in the units of grams of adsorbate per grams adsorbent and denote as x_m. The specific surface area, Σ, of the adsorbent in square meters per gram can be determined by

$$\Sigma = \frac{x_m}{M} N_A \sigma_m \times 10^{-20}, \qquad (3.1.20)$$

where M is the molar mass of the adsorbent and σ_m is area occupied by one molecule of adsorbent is square angstroms. With the assumption that the adsorbates have the same packing in their condensed phase, σ_m can be determined by

$$\sigma_m = 1.091 \left(\frac{M}{\rho N} \right)^{2/3}, \qquad (3.1.21)$$

where ρ is the the density(g Å^{-3}) and M is the molar mass of the adsorbate therefore allowing the surface area to be calculated with Equation 3.1.20.

15

3.2 Thermodynamics

3.2.1 Surface Thermodynamics

The conventional approach to describe the thermodynamics of a physical adsorption process is a 2D, surface thermodynamics treatment summarized in many sources [18–22]. This approach designates the adsorbed layer as a distinct phase on the surface of the adsorbent that is separated from the bulk adsorbate. This distinction can be made with the assumption that the adsorbent is thermodynamically inert, meaning that its properties are independent of the amount adsorbed and the temperature and pressure of the bulk adsorbate. This assumption was found to be reasonable for most cases of adsorption [23]. The exact location of the adsorbed and bulk phase boundary may be unknown, but at equilibrium, what is known is that the chemical potentials of adsorbed phase, μ_a, and the bulk phase, μ_g is equal. Therefore, assuming ideal gas behavior we have

$$\mu_a = \mu_g = \mu_g^\circ + RT \ln \left(\frac{P}{P^\circ} \right), \tag{3.2.1}$$

where μ_g° is the standard chemical potential at reference pressure P°. Differentiating by T at a constant number of moles adsorbed, n, and applying the Gibbs–Helmholtz relation yields

$$\frac{-\bar{\mathbf{H}}_a}{T^2} = \frac{-\bar{\mathbf{H}}_g^\circ}{T^2} + R \left(\frac{\partial \ln P}{\partial T} \right)_n \tag{3.2.2}$$

$$\left(\frac{\partial \ln P}{\partial T} \right)_n = \frac{\bar{\mathbf{H}}_g^\circ - \bar{\mathbf{H}}_a}{RT^2} = \frac{\bar{H}_g - \bar{\mathbf{H}}_a}{RT^2} = \frac{-\Delta H_a}{RT^2}. \tag{3.2.3}$$

The partial molar enthalpy, $\bar{\mathbf{H}}_g^\circ$, is equivalent to the molar enthalpy $\bar{H}_g$ in an ideal gas assumption. The quantity, $-\Delta H_a$ ($\equiv \bar{H}_g - \bar{\mathbf{H}}_a$) is the change in enthalpy of adsorption and is referred to as the isosteric heat of adsorption denoted as q_{st}. It is referred to

16

as the isosteric heat because q_{st} can also be expressed as

$$q_{st} = RT^2 \left(\frac{\partial \ln P}{\partial T} \right)_n = -R \left(\frac{\partial \ln P}{\partial (1/T)} \right)_n, \tag{3.2.4}$$

thus allowing for q_{st} to be found from isosteres, which are plots of $\ln(P)$ over the reciprocal temperature at constant a n. The isosteric heat may also be determined using calorimetry with good agreement [24].

It can also be shown that isosteres can be used to find the differential entropy of the adsorbed phase, $\bar{\mathbf{S}}_a$. With the assumption of an inert adsorbent with surface area A, the change in internal energy of the adsorbed phase can be written as

$$dU_a = TdS_a - PdV_a - \Pi dA + \mu_a dn_a, \tag{3.2.5}$$

where Π is the surface pressure, also referred to as the spreading pressure of the adsorbate. Taking the Gibbs free energy, G_a, to be defined as

$$G_a = U_a + PV_a - TS_a, \tag{3.2.6}$$

then,

$$dG_a = -S_a dT + V_a dP - \Pi dA + \mu_a dn_a \tag{3.2.7}$$

and taking the derivative with respect to n_a yields

$$d\mu_a = -\bar{\mathbf{S}}_a dT + \bar{\mathbf{V}}_a dP - \left(\frac{\partial \Pi}{\partial n_a} \right)_{P,T,A} dA + \left(\frac{\partial \mu_a}{\partial n_a} \right)_{P,T,A}$$
$$\bar{\mathbf{S}}_a = \left(\frac{\partial S_a}{\partial n_a} \right)_{P,T,A}, \bar{\mathbf{V}}_a = \left(\frac{\partial V_a}{\partial n_a} \right)_{P,T,A}. \tag{3.2.8}$$

Applying the case of a constant amount adsorbed with a fixed area to Equation 3.2.8

gives

$$d\mu_a = -\bar{\mathbf{S}}_a dT + \bar{\mathbf{V}}_a dP. \tag{3.2.9}$$

When the system is at equilibrium, the chemical potentials of the adsorbed phase and the bulk phase are equal, thus

$$-\bar{\mathbf{S}}_a dT + \bar{\mathbf{V}}_a dP = -\mathbf{S}_g dT + \mathbf{V}_g dP \tag{3.2.10}$$

or

$$dP = \left(\frac{\bar{S}_g - \bar{\mathbf{S}}_a}{\bar{V}_g - \bar{\mathbf{V}}_a}\right) dT, \tag{3.2.11}$$

where $\bar{S}_g$ and $\bar{V}_g$ is the molar entropy and molar volume of the bulk phase respectively. Lastly, with the assumptions of $\bar{V}_g \gg \bar{\mathbf{V}}_a$ and ideal gas Equation 3.2.11 becomes

$$\left(\frac{\partial \ln P}{\partial T}\right)_{n,A} = \frac{\bar{S}_g - \bar{\mathbf{S}}_a}{RT} \tag{3.2.12}$$

which, similarly to equation 3.2.4, can be applied to experimental isosteres to determine the differential entropy of the adsorbed phase. From rearrangement of Equation 3.2.12 we can also show the relationship of the differential entropy with the isosteric heat to be

$$T(\bar{S}_g - \bar{\mathbf{S}}_a) = RT^2 \left(\frac{\partial \ln P}{\partial T}\right)_{n,A} = -R\left(\frac{\partial \ln P}{\partial(1/T)}\right)_{n,A} = q_{st}. \tag{3.2.13}$$

Similarly to above, the molar entropy, $\bar{S}_a$ of the adsorbed phase may be found, but instead of isosteres, isotherms are used. To show this, a free energy, $F_a \equiv \mu_a\, n_a$, is defined which is equivalent to $F_a = G_a + \Pi A$. The derivative of F_a is thus

$$dF_a = \mu_a dn_a + n_a d\mu_a \tag{3.2.14}$$

and

$$dF_a = -S_a dT + V_a dP + A d\Pi + \mu_a dn_a. \tag{3.2.15}$$

Combining Equations 3.2.14 and 3.2.15 allows for $d\mu_a$ to be given as

$$d\mu_a = -\bar{S}_a dT + \bar{V}_a dP + \frac{1}{\Gamma} d\Pi, \tag{3.2.16}$$

where $\bar{V}_a$ is the molar volume and Γ, referred to as the surface excess, is defined as n_a/A.

As before, at equilibrium the chemical potentials are equal which gives

$$-\bar{S}_g dT + \bar{V}_g dP = -\bar{S}_a dT + \bar{V}_a dP + \frac{1}{\Gamma} d\Pi, \tag{3.2.17}$$

which at $d\Pi = 0$ gives

$$dP = \left(\frac{\bar{S}_g - \bar{S}_a}{\bar{V}_g - \bar{S}_a} \right) dT. \tag{3.2.18}$$

Applying the assumptions $\bar{V}_g \gg \bar{V}_a$ and ideal gas as before results in

$$\left(\frac{\partial \ln P}{\partial T} \right)_\Pi = \frac{\bar{S}_g - \bar{S}_a}{RT}, \tag{3.2.19}$$

which will allow for the determination of the molar entropy if the relationship between $\ln(P)$ and T at constant Π is known. This relationship can be determined from a series of isotherms by converting Equation 3.2.17 to a constant temperature situation, solving for $d\Pi$ and applying the assumptions used in Equation 3.2.19 to give the result of

$$d\Pi = \Gamma \left(\frac{RT}{P} \right) dP. \tag{3.2.20}$$

Writing the integral as

$$\Pi = RT \int_0^P \Gamma d(\ln P) \qquad (3.2.21)$$

shows that the spreading pressure my be found from area under curve of the isotherm which allows for the use of Equation 3.2.19 to determine the molar entropy.

We will end the review on surface thermodynamics with the definition of one more type of heat of adsorption called the equilibrium heat, $\Delta \bar{H}$, such that

$$\Delta \bar{H} = \bar{H}_g - \bar{H}_a = T(\bar{S}_g - \bar{S}_a), \qquad (3.2.22)$$

where $\bar{H}_g$ and $\bar{H}_a$ is the molar enthalpy of the bulk and adsorbed phase respectively. The relationship between the molar equilibrium heat of adsorption and the molar entropy is analogus to relationship of the isosteric heat with the differential molar entropy as shown below

$$T(\bar{S}_g - \bar{S}_a) = RT^2 \left(\frac{\partial \ln P}{\partial T} \right)_\Pi = \Delta \bar{H}, \qquad (3.2.23)$$

thus $\Delta \bar{H}$ is the heat of adsorption in a constant spreading pressure process. The relation between the thermodynamic quantities, q_{st}, $\bar{\mathbf{S}}_a$, $\bar{S}_a$, and $\Delta \bar{H}$, can be shown by addition and subtraction of $T\bar{\mathbf{S}}_a$ to equation 3.2.22 and substitution of 3.2.13 as shown below

$$\Delta \bar{H} = T(\bar{S}_g - \bar{S}_a + \bar{\mathbf{S}}_a - \bar{\mathbf{S}}_a) \qquad (3.2.24)$$

$$\Delta \bar{H} = q_{st} + T(\bar{\mathbf{S}}_a - \bar{S}_a). \qquad (3.2.25)$$

This section shows how differential and integral thermodynamic quantities can be determined from experimental data. The main assumption used to do so was

20

to consider the adsorbent to be inert and thus only depends of the surface area. Therefore allowing the adsorbate to be a distinct phase allowing for relations to the un adsorbed phase at equilibrium.

3.2.2   Solution Thermodynamics

Another approach for the description of the thermodynamic properties of a physical adsorption process is with solution thermodynamics. The advantages of this approach compared to surface thermodynamics is it results in functions for free energy, enthalpy, and entropy with pathways that are much easier to understand. Also, surface thermodynamics cannot be used for microporous adsorbents since the spreading pressure cannot be determined on the inside of a micropore. In this section a review of the application of solution thermodynamics for the process of physical adsorption described by Myers [25–27] is discussed.

The differences between surface and solution thermodynamics are actually quite small, as surface thermodynamics can be considered as a special case of solution thermodynamics when the adsorbent is considered to be inert. That assumption declares that the chemical potential of the adsorbent is independent of the amount adsorbed to it, thus allowing for internal energy of the adsorbed phase to be expressed as

$$U_a = TS_a - PV_a - \Pi A + \mu_a n_a, \tag{3.2.26}$$

which was found by subtracting the internal energy of the adsorbent from that of the system and inserting the ΠA term in place of the difference of the chemical potentials of the adsorbent. For solution thermodynamics, the approach is the same except the difference in the chemical potentials of the saturated adsorbent and the clean adsorbent is accounted for with the use of a term called the surface potential denoted

as Φ. The derivation of U_a is shown below.

The internal energy of the adsorbent with the adsorbate can be expressed as

$$U = TS - PV + \mu_a n_a + \mu m, \qquad (3.2.27)$$

where μ and m is the chemical potential and mass of the adsorbent. The internal energy of the clean adsorbent is

$$U_s = TS_s - PV_s + \mu_s, \qquad (3.2.28)$$

where S_s, V_s and μ_s are properties of the pure adsorbent. To simplify, the quantities in the above equation were converted to specific quantities and this convention will be followed for the rest of the section. The internal energy of the adsorbed phase is now acquired by subtraction of Equation 3.2.28 from Equation 3.2.27 to yield

$$U_a = TS_a - PV_a + \mu_a n_a + \Phi, \qquad (3.2.29)$$

where

$$\Phi = \mu - \mu_s, \qquad (3.2.30)$$

thus Φ takes the place of ΠA. The surface potential can be determined just as was done for the spreading pressure by integration of the Gibbs adsorption isotherm [28],

$$d\Phi = -n_a RT \, d\ln P$$
$$\Phi = -RT \int_0^P n_a \, d\ln P \qquad (3.2.31)$$

and comparison with Equation 3.2.21 shows that $\Phi = -\Pi A$.

In the solution thermodynamic treatment of adsorption, the Gibbs model of ad-

sorption is used. In the Gibbs model the adsorbed layer is considered part of the adsorbent creating an infinitesimally thin boundary layer separating the bulk gas and adsorbent illustrated in Figure 3.2. From now on properties with the subscript a, will correspond to the conditions at the boundary layer.
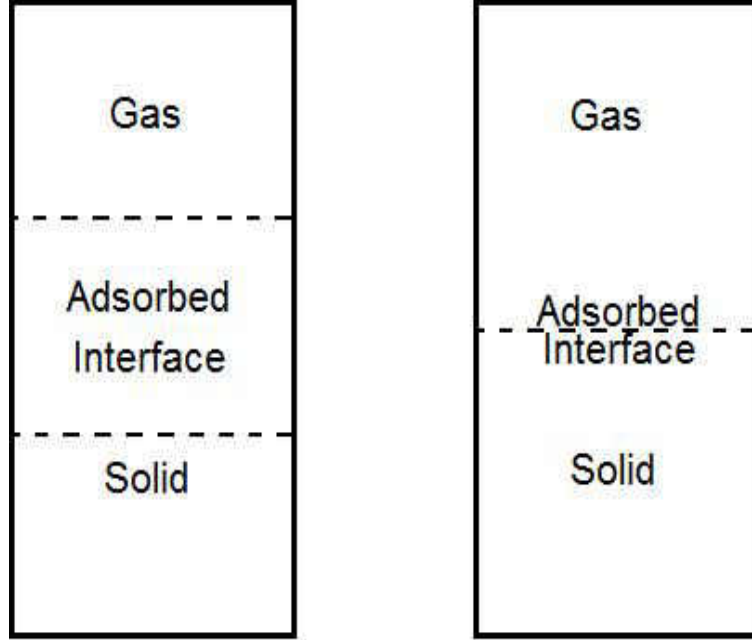
Figure 3.2. Comparison of actual adsorption model (Left) with the Gibbs model (Right).

Applying the Gibbs model and Equation 3.2.29 the state functions of the boundary layer can be expressed as

$$
\begin{aligned}
U_a &= TS_a + \mu_a n_a + \Phi \\
H_a &= TS_a + \mu_a n_a + \Phi \\
A_a &= \mu_a n_a + \Phi \\
G_a &= \mu_a n_a + \Phi.
\end{aligned}
\tag{3.2.32}
$$

Since the boundary is infinitesimally thin, $V_a = 0$, therefore the internal energy is equal to the enthalpy and the Helmholtz free energy is equal to the Gibbs free en-

ergy. Similarly, from the fundamental thermodynamic relation for a constant mass of adsorbent the differential state functions for the boundary layer can be expressed as

$$dU_a = TdS_a + \mu_a dn_a$$
$$dH_a = TdS_a + \mu_a dn_a$$
$$dA_a = -SdT_a + \mu_a dn_a$$
$$dG_a = -SdT_a + \mu_a dn_a.$$

(3.2.33)

We now move to showing how to derive useful integral functions for the Gibbs free energy, enthalpy, and entropy of the boundary that can be determined experimentally to allow for characterization of adsorbents. The functions are given relative to an ideal gas reference at the same temperature

$$\Delta G_a = G_a - \mu^\circ n_a$$
$$\Delta H_a = H_a - h^\circ n_a$$
$$\Delta S_a = S_a - s^\circ n_a,$$

(3.2.34)

where μ°, h°, and s° are molar quantities of the ideal gas reference state. We still need an expression for the entropy of the boundary layer. Differentiating the Gibbs free energy in Equation 3.2.32 with help from Equation 3.2.33 and solving for $d\Phi$ yields

$$d\Phi = -S_a dT - n_a d\mu_a.$$

(3.2.35)

Now solving for the entropy of the adsorbed layer and applying the appropriate Maxwell relation [29] gives

$$S_a = n_a \bar{s}_g - \frac{\partial \Phi}{\partial T},$$

(3.2.36)

24

where at equilibrium, $\mu_a = \mu_g$, $\bar{s}_g$ is the partial molar entropy of the bulk gas. Now, expressions for G_a and S_a can be substituted into Equation 3.2.34 and ΔH_a solved for from $\Delta H_a = \Delta G_a - \Delta S_a$ to yield

$$\Delta G_a = (\mu_g - \mu^\circ)n_a + \Phi$$
$$\Delta H_a = (\bar{h}_g - h^\circ)n_a + \Phi - T\frac{\partial \Phi}{\partial T} \qquad (3.2.37)$$
$$\Delta S_a = (\bar{s}_g - s^\circ)n_a - \frac{\partial \Phi}{\partial T},$$

The functions of Equation 3.2.37 are the sum of the result from two changes of the adsorbate, the first being isothermal compression of the adsorbate from the ideal gas reference state, and the second being the immersion of the adsorbent into the compressed adsorbate.

$$\Delta G_a = \Delta G_{comp} + \Delta G_{imm}$$
$$\Delta H_a = \Delta H_{comp} + \Delta H_{imm} \qquad (3.2.38)$$
$$\Delta S_a = \Delta S_{comp} + \Delta S_{imm}$$

To show this, consider an expression for the free energy of immersion to be the sum of the differences of the free energies of the adsorbate at the boundary layer from those in the bulk phase, and the free energies of the adsorbent, G_s, from a clean (under vacuum) adsorbent, G_{s*}.

$$\Delta G_{imm} = (G_a - \mu_g n_a) + (G_s - G_{s*}) \qquad (3.2.39)$$

With use of Equation 3.2.32 and assuming the differences of the free energies of the adsorbent is negligible, we have

$$\Delta G_{imm} = \Phi, \tag{3.2.40}$$

and applying the same treatment for enthalpy and entropy of immersion yields

$$\Delta H_{imm} = \Phi - T\frac{\partial \Phi}{\partial T}$$
$$\Delta S_{imm} = -\frac{\partial \Phi}{\partial T}. \tag{3.2.41}$$

Removal of the immersion functions from Equation 3.2.37 leaves expressions for the the compression functions.

$$\Delta G_{comp} = (\mu_g - \mu^\circ)n_a$$
$$\Delta H_{comp} = (\bar{h}_g - h^\circ)n_a \tag{3.2.42}$$
$$\Delta S_{comp} = (\bar{s}_g - s^\circ)n_a$$

which for an ideal gas converts to

$$\Delta G_{comp} = RTn_a \ln \frac{P}{P\circ}$$
$$\Delta H_{comp} = 0 \tag{3.2.43}$$
$$\Delta S_{comp} = -Rn_a \ln \frac{P}{P\circ}.$$

The molar integral functions, Δg_a, Δh_a, and Δs_a, are obtained by dividing the integral functions by n_a.

$$\Delta g_a = \frac{\Delta G_a}{n_a}$$

$$\Delta h_a = \frac{\Delta H_a}{n_a} \qquad (3.2.44)$$

$$\Delta s_a = \frac{\Delta S_a}{n_a}$$

Substitution of Equation 3.2.44 into Equation 3.2.34 and differentiating yields

$$\Delta \bar{g}_a = \mu_a - \mu^\circ = RT \ln\left(\frac{P}{P^\circ}\right)$$

$$\Delta \bar{h}_a = \bar{h}_a - h^\circ = -RT^2\left(\frac{\partial \ln P}{\partial T}\right) \qquad (3.2.45)$$

$$\Delta \bar{s}_a = \bar{s}_a - s^\circ = R\left(\ln\frac{P}{P^\circ} - T\frac{\partial \ln P}{\partial T}\right),$$

where $\Delta \bar{g}_a$, $\Delta \bar{h}_a$, and $\Delta \bar{s}_a$ are differential functions. Another connection with the surface thermodynamic approach can be made by comparison of the differential enthalpy with the isosteric heat, Equation 3.2.4, shows that $\Delta \bar{h}_a = -q_{st}$.

From the comparison of surface and solution thermodynamics approaches it can be seen that solution thermodynamics provides more physically understandable properties of the adsorption process. Obviously the two approaches are connected, but for the case of hydrogen adsorption into COFs, solution thermodynamics is the better choice.

3.3 Excess and Absolute Properties

To quantify the amount of hydrogen adsorbed, the H_2 uptake can be expressed as either excess or total uptake. Excess uptake is defined as the amount of H_2 present within the pore volume of the absorbent beyond which would be present in the pore volume had adsorption not taken place. This is also referred to as the hydrogen that is actually bound to the surface of the absorbent, whereas total uptake refers to the total amount of H_2 present within pore volumes. These two types are essentially identical at atmospheric pressures, but deviate from each other as pressure increases or decreases. Likewise the thermodynamic properties of the system can refer to either excess or absolute properties. Experimental measurements of adsorption result in excess properties, whereas when simulation methods are used, the measurement is the total adsorption. The conversion of any absolute thermodynamic property, X, to the excess, X_e, or the other way around, can be performed with Equation 3.3.1 if the molar density, ρ_g, total volume, V_g, and molar property, x_g, of the gas is known [30].

$$X = X_e + \rho_g V_g x_g \qquad (3.3.1)$$

The properties with subscript a in the previous section correspond to excess properties. For the immersion properties, it makes the most sense to express as excess properties since these would allow the adsorbent to be properly thermodynamically evaluated. In terms of the practical application of H_2 storage materials, the absolute uptake is what should be maximized. The excess amount adsorbed is sometimes given in reports. This does provide some insight to the adsorbents abilities, but in terms of the DOE targets in Table 1.1 the absolute uptake of H_2 is what matters.

CHAPTER 4

HYDROGEN ADSORPTION MODELING

Currently, there are very few reports available that contain experimental data on the adsorption of hydrogen into COFs. Besides COFs being relatively new materials, this is attributed to the existence of numerous problems with obtaining accurate experimental results. One such issue to cope with is the presence of impurities and imperfections in the framework of the absorbent as well as impurities present in the absorbate. Careful synthesis of the COF and the implementation of a liquid nitrogen trap in the hydrogen supply line are two techniques used to reduce the presence of impurities. Another issue with experimental methods is that the results are given as excess adsorption as opposed to the total adsorption which is the desired measurement in determining practical applications. Therefore the pore volume of the absorbent must also be determined through further experimentation to allow the use of Equation 3.3.1. However, this in itself is not the main issue, as it has been observed that when H_2 is confined within the pores of the material it may not have the same density as the density of the bulk H_2 [31]. Even a small variation in the densities of the bulk H_2 and the H_2 confined within the pores leads to large errors in the total uptake because of the large pore volumes of the adsorbent material. Yet another issue present is the difficulty of completely degassing the absorbent. Careful experimentation of degassing at certain temperatures along with the use of an ultra-high vacuum can correct this issue. Correction of all these problems as a whole requires very time

consuming experimentation, not to mention the need for specialized instruments.

Despite the problems present in the experimental determination of hydrogen adsorption into COFs, it is essential that experiments be carried out if COFs are ever to be used in practical applications. Many of the reports containing experimental results of H_2 adsorption into COFs are from Yaghi *et al.* [32, 33]. In both studies, adsorption isotherms were obtained using a gravimetric measurement. Gravimetric methods are typically used for high pressure measurements (1-100 bar) and volumetric measurements are preformed at low pressures (>1 bar). However, an experimental method for the measurement of H_2 adsorption into COF-1 using static volumetric techniques has been described by Y. Li and R. T. Yang [34]. Both methods are still exposed to the previously described issues and require careful and time consuming work to create adsorption isotherms.

4.1   Quantum Mechanics

Given the constraints of collecting experimental data, the use of simulation methods is the dominant technique used to determine the hydrogen adsorption abilities of COFs. A first-principles based study is the general approach that has been used in theoretical studies of not only hydrogen adsorption into COFs but also hydrogen adsorption into other porous materials as well. This method is simply described as the use of first-principles calculations to determine the potential energies of the interactions of hydrogen molecules with the framework. The results from these calculations are used to determine the force field parameters. This allows for grand canonical Monte Carlo (GCMC) simulations to generate hydrogen adsorption isotherms. The details of different quantum methods will be the rest of the content of this section.

4.1.1 Density Functional Theroy

The goal of all methods is to provide a solution to the Schrödinger equation as accurately as possible. The Schrödinger equation is an eigenvalue equation that describes the quantum state of the system shown below as

$$\hat{H}\Psi = E\Psi, \tag{4.1.1}$$

where $\hat{H}$ is the Hamiltonian operator, Ψ is the wavefunction and E is the corresponding energy. The Hamiltonian represents the total energy of the system which is broken down to the sum of the kinetic and potential energies. This is shown mathematically as

$$\hat{H} = -\frac{\hbar^2}{2m}\nabla^2 + V(r), \tag{4.1.2}$$

The potential energy is a result of Coulombic interactions of the nuclei and electrons, and for a system of M atoms and N electrons the complete Hamiltonian is expressed in atomic units as

$$\hat{H} = -\sum_{i}^{N}\frac{1}{2}\nabla_i^2 - \sum_{A}^{M}\frac{1}{2M_A}\nabla_A^2 - \sum_{A}^{M}\sum_{i}^{N}\frac{Z_A}{r_{iA}} + \sum_{A}^{M-1}\sum_{B>A}^{M}\frac{Z_AZ_B}{r_{AB}} + \sum_{i}^{N-1}\sum_{i<j}^{N}\frac{1}{r_{ij}}, \tag{4.1.3}$$

where M_A is the ratio of the mass of the Ath nucleus to the mass of an electron and Z_A the atomic number of nucleus A. The first and second terms of the above equation represent the kinetic energy of the electrons and the nuclei. The third term accounts for the attraction between the electrons and the nuclei. The last two terms correspond to the nuclei-nuclei and the electron-electron repulsion. Solving the Schrödinger equation with this Hamiltonian cannot be done, therefore some approximations must be made. First and foremost, due to the relatively large mass of the nuclei in compari-

son to the electrons, the nuclei are in a fixed position with respect to the fast moving electrons. This is called the Born-Oppenheimer approximation and its application is standard in quantum mechanics. With this approximation, two terms drop out of the Hamiltonian to yield

$$\hat{H}_{elec} = -\frac{1}{2}\sum_i^N \nabla_i^2 - \sum_A^M \sum_i^N \frac{Z_A}{r_{iA}} + \sum_i^{N-1} \sum_{j>i}^N \frac{1}{r_{ij}}, \qquad (4.1.4)$$

which is referred to as the electronic Hamiltonian.

It is from this point where the quantum methods begin to differ, even with the Born-Oppernheimer approximation, the Schrödinger equation cannot be solved for systems with two or more electrons thus more approximations are needed.

One approach, termed density functional theory (DFT), is to define the energy of the system as functionals (functions with vector inputs and scalar outputs) of electron density, $\rho(\mathbf{r})$, thus converting a multi-body problem into a single body one. The prominent developments to DFT came from the work of Hohenburg, Kohn, and Sham [35, 36]. They showed how the energy of the system is a functional of the electron density and can be expressed as

$$E[\rho] = \int V(\mathbf{r})\rho(\mathbf{r})d\mathbf{r} + F[\rho], \qquad (4.1.5)$$

where $V(r)$ is the electron-nuclei interaction and $F[\rho]$, the unknown of the equation, is a functional that contains the electronic repulsions and kinetic energies. Some known quantities can be separated out from this unknown functional to give

$$F[\rho] = \frac{1}{2}\int\int \frac{\rho(\mathbf{r})\rho(\mathbf{r}^*)}{|\mathbf{r} - \mathbf{r}^*|}d\mathbf{r}d\mathbf{r}^* + T_s[\rho] + E_{xc}[\rho], \qquad (4.1.6)$$

where the first term is Coulomb repulsion of the electrons, $T_s[\rho]$ is the kinetic energy of the system if electron interactions are ignored, and $E_{xc}[\rho]$ is the remaining unknown termed the exchange and correlation energy. A common approximation of

32

the exchange and correlation energy functional, known as the local-density approx-imation (LDA), is to model the system as a uniform electron gas [37]. This allows the functional to be expressed as the sum of exchange and correlation energy per electron, $\epsilon_{xc}(\rho(\mathbf{r}))$, such that

$$E_{xc}[\rho] = \int \rho(\mathbf{r})\epsilon_{xc}(\rho(\mathbf{r}))d\mathbf{r}. \tag{4.1.7}$$

Of course, now an expression for $\epsilon_{xc}(\rho(\mathbf{r}))$ is required. There is no known analytical expression for the per electron correlation energy, ϵ_c and approximations of it vary, but exchange energy is known thus $\epsilon_{xc}(\rho(\mathbf{r}))$ can be written as

$$\epsilon_{xc}(p) = -\frac{3}{4}\left(\frac{3\rho(\mathbf{r})}{\pi}\right)^{1/3} + \epsilon_c. \tag{4.1.8}$$

The variational method can now be applied to determine the ground state energy of the system. The variational method uses the theorem that the approximated energy determined from normalized wavefunctions will always be greater than the exact energy. Thus the upper bound of the ground state energy can be determined by minimization, mathematically expressed as

$$\int \partial\rho(\mathbf{r})V_{eff}(\mathbf{r})d\mathbf{r} = 0$$

$$(4.1.9)$$

$$V_{eff}(\mathbf{r}) = V(\mathbf{r}) + \int \frac{\rho(r^*)}{|\mathbf{r}-\mathbf{r}^*|}d\mathbf{r}^* + \frac{\partial T_s[\rho]}{\partial\rho(\mathbf{r})} + \frac{\partial\rho(\mathbf{r})\epsilon_{xc}(\rho(\mathbf{r}))}{\partial\rho(\mathbf{r})}.$$

The connection between the noninteracting system with the real system is that the real system is the noninteracting system exposed to an effective external potential,V_{eff}, such that $\rho_s(\mathbf{r}) = \rho(\mathbf{r})$. This allows for the electron density to determined by solving the Kohn-Sham equations.

$$\left(-\frac{1}{2}\nabla^2 + V_{eff}(\mathbf{r}) \right) \psi_i(\mathbf{r}) = \epsilon_i \psi_i(\mathbf{r}) \qquad (4.1.10)$$

$$\rho(\mathbf{r}) = \sum_{i=1}^{N} |\psi_i(\mathbf{r})|^2 \qquad (4.1.11)$$

Starting with an assumed $\rho(\mathbf{r})$, the new $\rho(\mathbf{r})$ of the minimized system is found iteratively and the ground state energy of the system is given as

$$E = \sum_{i=1}^{N} \epsilon_i - \frac{1}{2} \int \int \frac{\rho(\mathbf{r})\rho(\mathbf{r}^*)}{|\mathbf{r} - \mathbf{r}^*|} d\mathbf{r} d\mathbf{r}^* + \int \rho(\mathbf{r}) \left[\epsilon_{xc}(\rho(\mathbf{r})) - \frac{\partial \epsilon_{xc}(\rho(\mathbf{r}))}{\partial \rho(\mathbf{r})} \right] d\mathbf{r}. \quad (4.1.12)$$

Another commonly used approximation for the exchange-correlation energy is the generalized gradient approximation. However in practice, it is common to model the exchange-correlation energy as a linear combination of various approximations referred to as hybrid functionals.

The process of determining force field parameters usually begins with (DFT) calculations for the determination of adsorption sites. These calculations result in approximate binding energies and the orientation of hydrogen with the framework. The COF unit cell is much too large of a system for even the simplest of calculations and therefore must be broken down into several different pieces that as a whole represent the COF. For instance, the fragments of COF-102, COF-103, COF-105, and COF-108 shown in Figure 4.1 were used in a study performed by Cao *et al.* [41]. The geometries of the fragments were first optimized through the use of the hybrid functional B3LYP with 6-31G* basis set. Then to determine the preferred hydrogen adsorption site of each fragment, the binding energies of H$_2$ to the fragments is calculated using the PW91 functional with the 6-311G* basis set.
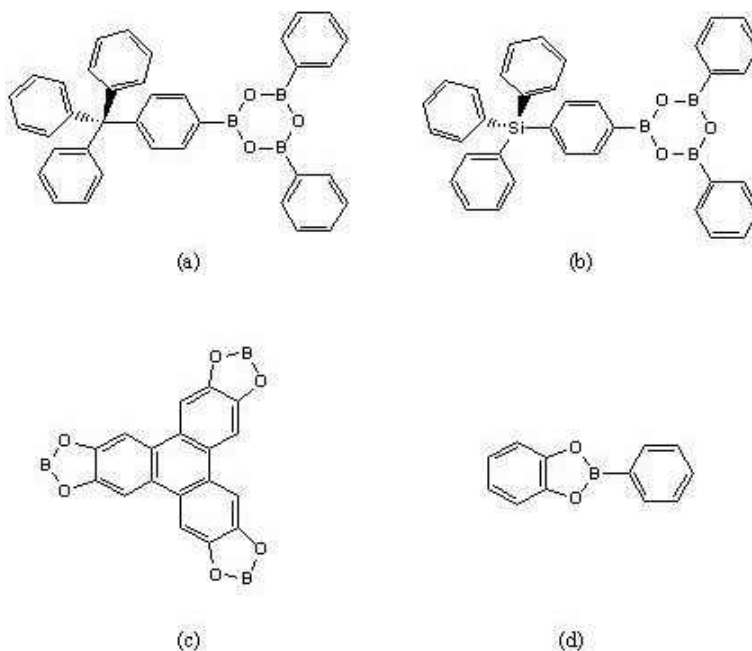
Figure 4.1. COF Fragments

4.1.2 Hartree-Fock

From the results of the DFT calculations, the interaction energies can be determined from Hartree-Fock calculations. These types of calculations are used instead of DFT because DFT methods are not accurate when considering long range dispersion interactions [38]. Like DFT, Hartree-Fock methods make use of the Born-Oppernheimer approximation to simplify the Hamiltonian. However, instead of converting from a multi-body to a single body problem to solve the Schrödinger equation, the Schrödinger equation is solved for many single body problems. In other words, the Hartree-Fock method determines the best one-electron-orbitals, ψ_i, then combines them to give an estimate for the ground state wavefunction [39]. To be able to split the problem into single body problems, there has to be a way to account for the electron-electron repulsion terms, the solution being the use of the mean field approximation which uses an average charge of all the other electrons to calculate the repulsive term for the one electron in question. Thus we have a one electron Hamiltonian which is termed the Fock operator shown below for the i-th electron as

$$\hat{F}(i) = -\frac{1}{2}\nabla_i^2 - \sum^M \frac{Z_a}{r_{ia}} + \sum^{N/2} [2\hat{J}_j - \hat{K}_j], \qquad (4.1.13)$$

where $\hat{J}_j$ is the Coulombic operator that describes the electron-electron repulsion of the i-th and j-th electrons, and $\hat{K}_j$ is the exchange operator that describes the exchange of electrons potential. Now the single body Schrödinger equation to be solved for each electron is

$$\hat{F}\psi_i = \epsilon_i \psi_i. \qquad (4.1.14)$$

The variational method is then used to determine functions for orbitals to obtain the lowest possible energy which is closest to the exact solution of the multi-body Schrödinger equation. Once the complete set of orbitals is determined, they can be combined to give the ground state wavefunction, Ψ. Originally the wavefunction was given be the product of the orbitals referred to as the Hartree product. However, this does not include spin orbitals. Inclusion of spin orbitals, χ_i, and to make them antisymmetric can be achieved with a Slater determinant which for the case of two electrons is given as

$$\Psi = \frac{1}{\sqrt{2}} [\chi_1(\psi_1)\chi_2(\psi_2) - \chi_1(\psi_2)\chi_2(\psi_1)] \qquad (4.1.15)$$

or for an N electron system

$$\Psi = \frac{1}{\sqrt{N!}} \begin{vmatrix} \chi_1(\psi_1) & \chi_2(\psi_1) & \cdots & \chi_N(\psi_1) \\ \chi_1(\psi_2) & \chi_2(\psi_2) & \cdots & \chi_N(\psi_2) \\ \vdots & \vdots & \ddots & \vdots \\ \chi_1(\psi_N) & \chi_2(\psi_N) & \cdots & \chi_N(\psi_N) \end{vmatrix}. \qquad (4.1.16)$$

Thus we now have an approximation of the ground state wavefunction.

The difference in the Hartree-Fock and exact energies termed the correlation en-

ergy can be large enough to result in deviations from experiments.

4.1.3 Møller-Plesset Perturbation Theory

Improvements to the Hartree-Fock method can be made by somehow accounting for the correlation energy. Methods of this type are referred to as post-Hartree-Fock methods and an example of these methods is Møller-Plesset perturbation theory (MP). This approach is based on Rayleigh-Schroedinger perturbation theory which solves the Schrödinger equation by splitting the Hamiltonian into a known reference, $\hat{H}_0$, and a perturbation term, $\hat{V}$, shown below as

$$\hat{H} = \hat{H}_0 + \lambda \hat{V},$$

(4.1.17)

where λ is a parameter that defines the extent of perturbation [40]. The energy and wavefunction can thus be expressed as a power series to order m as

$$E = \sum_{i=0}^{m} \lambda^i E^{(n)}$$
$$\psi = \sum_{i=0}^{m} \lambda^i \psi^{(n)}.$$

(4.1.18)

These can then be substituted into the Schrödinger equation and separated into like powers such that

$$\hat{H}_0 \psi^{(0)} 0 = E^{(0)} \psi^{(0)}$$

$$\hat{H}_0 \psi^{(1)} + \hat{V} \psi^{(0)} = E^{(0)} \psi^{(1)} + E^{(1)} \psi^{(0)}$$

$$\hat{H}_0 \psi^{(2)} + \hat{V} \psi^{(1)} = E^{(0)} \psi^{(2)} + E(1) \psi^{(1)} + E^{(2)} \psi^{(0)} \qquad (4.1.19)$$

$$\vdots$$

$$\hat{H}_0 \psi^{(m)} + \hat{V} \psi^{(m-1)} = E^{(0)} \psi^{(m)} + E_1 \psi^{(k-1)} \cdots + E^{(m)} \psi^{(0)}.$$

Multiplying Equation 4.1.19 by $\langle \psi^{(0)} |$ and integrating gives the following expressions for the perturbation energies

$$E^{(0)} = \langle \psi^{(0)} | \hat{H}_0 | \psi^{(0)} \rangle$$

$$E^{(1)} = \langle \psi^{(0)} | \hat{V} | \psi^{(0)} \rangle$$

$$E^{(2)} = \langle \psi^{(0)} | \hat{V} | \psi^{(1)} \rangle \qquad (4.1.20)$$

$$\vdots$$

$$E^{(m)} = \langle \psi^{(0)} | \hat{V} | \psi^{(m-1)} \rangle.$$

Now for MP the unperturbed reference Hamiltonian is the sum of the one electon Fock operator and the perturbation is the correlation energy. For zero order MP(MP0), $E^{(0)}$ is the sum of the electron energies neglecting electonic repulsion. The MP1 perterbation energy, $E^{(1)}$, is the Hartree-Fock correlation energy, thus the MP1 energy $(E^{(0)} + E^{(1)})$ is the same as the Hartree-Fock energy. Therefore MP2 is the lowest order that results in an improvement to Hartree-Fock.

Typically second-order Møller-Plesset calculations are used to determine the parameters for the force field [32, 41–43]. The results for the DFT calculations determined the adsorption geometries which are used in the MP2 calculations. The fragments used in the DFT calculations(Figure 4.1) are too large for MP2 calcula-

tions and were broken down into smaller clusters shown in Figure 4.2 that contain only the closest atoms to hydrogen adsorption site.
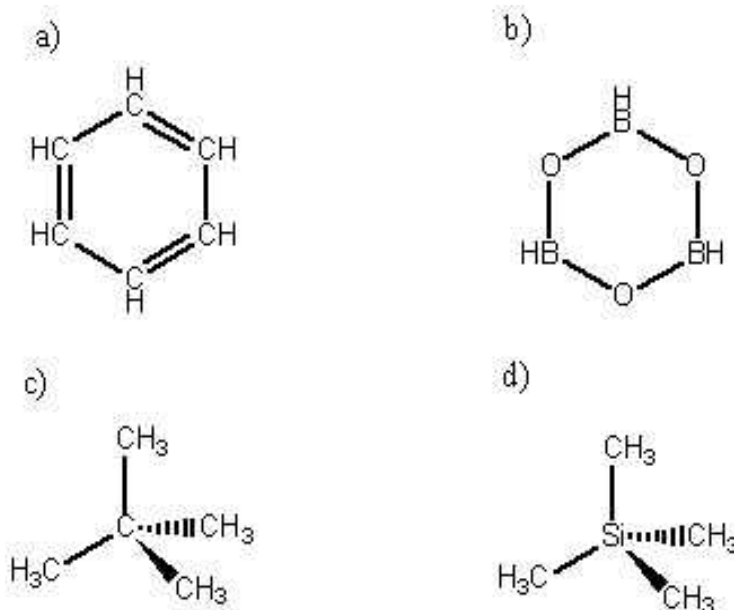
Figure 4.2. COF Clusters

4.2 Grand Canonical Monte Carlo

Results from the quantum mechanics calculation now allow the use of GCMC simulations to create isotherms of hydrogen adsorption into the framework. The grand canonical ensemble is commonly used for adsorption studies because it allows the energy and the number of particles of the system to change while holding volume, temperature, and chemical potential constant. GCMC simulations are random samplings of the system by performing four types of trial movements which attempt to find the lowest possible energy configuration. The trial moves are: creation of a particle at a randomly chosen position, removal of a randomly chosen particle, random particle displacement, and rotation of particle. After each movement, the energy of the system is compared with the previous energy of the system and then the move

is either accepted or rejected. The energy of the system is determined from the collection of mathematical functions referred to as the force field. In our case, the parameters of the force field are determined from the results of MP2 calculations. The force field parameters are commonly input into the Morse potential (Equation 4.2.1), but the Lennard-Jones potential (Equation 4.2.2) is also sometimes used to cut down on computational cost. Besides the need of a force field, the representation of the COF must also be defined. The position of the atoms of the COF are fixed throughout the simulation and to control boundary effects, the COF is represented as a periodic super cell model where each super cell represents a cube of eight unit cells [32].

$$U(r_{ij}) = D \left[\exp \left(\alpha \left[1 - \frac{r_{ij}}{r_0} \right] \right) - 2\exp \left(\frac{\alpha}{2} \left[1 - \frac{r_{ij}}{r_0} \right] \right) \right] \qquad (4.2.1)$$

$$V_{LJ} = 4\varepsilon \left[\left(\frac{\sigma}{r} \right)^{12} - \left(\frac{\sigma}{r} \right)^{6} \right] \qquad (4.2.2)$$

4.3 Expanded Wang-Landau

An alternative to GCMC is the more recently developed Wang-Landau (WL) method [44, 45]. Contrary to GCMC, the WL method directly determines the density of states instead of calculating the properties of the system at a given set of conditions. This allows for the determination of adsorption isotherms to be done in one simulation. Also, all the thermodynamic properties of the system can be calculated, specifically the immersion and desorption Gibbs free energies. Given these advantages over GCMC, we used the WL method to study the adsorption of hydrogen into COFs. The remainder of this section describes the implementation of the method in detail.

As stated above, the WL method determines the density of states of the system

which in turn allows for the calculation of the grand-canonical partition function shown below as

$$\Theta\left(\mu, V, T\right) = \sum_{N=0}^{\infty} Q\left(N, V, T\right) \exp\left(\beta \mu N\right), \tag{4.3.1}$$

where $\beta = 1/ k_B T$, μ is the chemical potential, and Q(N, V, T) is the canonical partition function which will be calculated by

$$Q\left(N, V, T\right) = \frac{V^N}{N! \Lambda^{3N}} \int \exp\left(-\beta U\left(\Gamma\right) d\Gamma\right), \tag{4.3.2}$$

where Λ is the De Broglie wavelength and U(Γ) is the energy of a specific configuration of the atoms in the system.

Determination of the grand-canonical partition function requires sampling for varying N, therefore a way change the number of molecules in the system is needed. The addition or removal of a molecule in one Monte Carlo step can be too abrupt of a change and result in inadequate sampling especially for condensed phases. Instead, the addition or removal of a molecule is broken up into M steps through the introduction of a fractional molecule l where $l = \mathbb{Z}_M$. The use of this insertion method with WL is what is referred to as expanded Wang-Landau simulations [46, 47]. With this method, we are now in the expanded grand-canonical ensemble and as a result have a more complicated partition function to deal with. However, since only the grand-canonical partition function is desired and with the assumption that the mass of the fractional molecule is equal to mass of a full molecule, a simplified expanded grand-canonical (SEGC) partition function can be used.

$$\Theta_{\text{SEGC}} = \sum_{N=0}^{\infty} \sum_{l=0}^{M-1} Q\left(N, V, T, l\right) \exp\left(\beta \mu N\right) \tag{4.3.3}$$

where

$$Q\left(N,V,T,l\right) = \frac{V^{N+1}}{N!\Lambda^{3(N+1)}} \int \exp\left(-\beta U\left(\Gamma\right)\right) d\Gamma, 0 < l < M \qquad (4.3.4)$$

In order to determine the SEGC partition function, the system must be sampled at all (N,l) values. Doing so requires the use of a biased distribution function, specifically one that increases the probability to visit a (N,l) value that has not been visited. This biased distribution is defined as $p_{bias} = p(\Gamma,N,l)/p(N,l)$ where $p(\Gamma,N,l)$ and $p(N,l)$ are given below

$$p(\Gamma, N, l)$$
$$= \frac{V^{N+1}\exp(\beta\mu N - \beta U(\Gamma))}{N!\Lambda^{3(N+1)}\Theta_{\text{SEGC}}(\mu, V, T)}, 0 < l < M \qquad (4.3.5)$$
$$= \frac{V^{N}\exp(\beta\mu N - \beta U(\Gamma))}{N!\Lambda^{3N}\Theta_{\text{SEGC}}(\mu, V, T)}, l = 0$$

$$p(N, l) = \int p(\Gamma, N, l)d\Gamma = \frac{Q(N, V, T, l)\exp(\beta\mu N)}{\Theta_{\text{SEGC}}(\mu, V, T)}. \qquad (4.3.6)$$

From this biased distribution, the general acceptance criterion to move from original state (Γ_o, N_o, l_o) to a new state (Γ_n, N_n, l_n) for a Metropolis algorithm is

$$acc(o \to n) = min\left[1, \frac{p_{\text{bias}}(\Gamma_n, N_n, l_n)}{p_{\text{bias}}(\Gamma_o, N_o, l_o)}\right], \qquad (4.3.7)$$

which is fully written out as

$$acc(o \to n)$$

$$= min\left[1, \frac{Q(N_o,V,T,l_o)V^{N_n}N_o!\Lambda^{3N_o}\exp(-\beta U(\Gamma_n))}{Q(N_n,V,T,l_n)V^{N_o}N_n!\Lambda^{3N_n}\exp(-\beta U(\Gamma_o))}\right], \begin{array}{l} l_o = 0 \text{ and } l_n = 0 \text{ or} \\ l_o > 0 \text{ and } l_n > 0 \end{array}$$

$$= min\left[1, \frac{Q(N_o,V,T,l_o)V^{N_n+1}N_o!\Lambda^{3N_o}\exp(-\beta U(\Gamma_n))}{Q(N_n,V,T,l_n)V^{N_o}N_n!\Lambda^{3(N_n+1)}\exp(-\beta U(\Gamma_o))}\right], l_o = 0 \text{ and } l_n > 0$$

$$= min\left[1, \frac{Q(N_o,V,T,l_o)V^{N_n}N_o!\Lambda^{3(N_o+1)}\exp(-\beta U(\Gamma_n))}{Q(N_n,V,T,l_n)V^{N_o+1}N_n!\Lambda^{3N_n}\exp(-\beta U(\Gamma_o))}\right], l_o > 0 \text{ and } l_n = 0.$$

$$(4.3.8)$$

The exponential term is given from the force field and allows configurations of favorable energy to be accepted. The $Q(N,V,T,l)$ terms impose a penalty for visiting a previously visited (N,l) configuration, thus allowing the system to sample all values of (N,l). From this acceptance criterion and setting an initial value of $Q(N,V,T,l) = 1$ for all N and l the metropolis algorithm can proceed. As the simulation progresses, each time a configuration with (N,l) particles is visited, the value of $Q(N,V,T,l)$ is updated by $\ln(f)$, where f is a convergence factor greater than one. A histogram of the number of visits for each (N,l) is kept and is monitored to determine when to stop the algorithm. This ensures that appropriate sampling for each (N,l) occurs. Once the histogram is adequately flat, the convergence factor f is reduced and simulation restarts with a new histogram. This process is repeated until a threshold value of f is reached. Repeating this process to an convergence factor close to 1 results in an accurate estimate of $Q(N,V,T,l = 0)$ for all N which is used in Equation 4.3.1 to determine the grand-canonical partition function for any chemical potential.

Once the grand-canonical partition function is found, the probability of N molecules adsorbed into the COF is determined by

$$p(N) = \frac{Q(N,V,T)\exp(\beta\mu N)}{\Theta(\mu,V,T)}, \tag{4.3.9}$$

which can then be used in Equation 4.3.10 to calculate the absolute amount adsorbed, N_a. Now the internal energy of the adsorbate can be calculated with Equation 4.3.11 from the sum of the average potential energy of an adsorbed molecule, $\overline{E}_{pot}(N)$, and the kinetic energy of an ideal gas with five (two rotational) degrees of freedom.

$$N_a = \sum_{N=0}^{\infty} Np(N) \tag{4.3.10}$$

$$U = N_a \frac{\sum_N (\overline{E}_{pot}(N) + (5/2)k_BT)p(N)}{\sum_N p(N)} \tag{4.3.11}$$

Use of the grand-canonical partition function to determine other various thermodynamic properties can be shown after first introducing the characteristic state function of the grand canonical ensemble referred to as the grand potential, denoted as Ω and defined below as

$$\Omega = U - TS - \mu N. \tag{4.3.12}$$

From the fundamental thermodynamic relation the grand potential can also be written as

$$\Omega = -PV. \tag{4.3.13}$$

The relation between the grand potential and the grand canonical partition function is given in Equation 4.3.14 [48].

$$\Omega = -k_BT\ln\Theta(\mu,T,V) \tag{4.3.14}$$

From this relation to the grand canonical partition function, the thermodynamic properties of the system can be calculated. First, the pressure of the adsorbate at a given μ can be determined as

$$P = \frac{k_B T \ln \Theta(\mu, T, V)}{V}.$$ (4.3.15)

The other important state functions can be calculated as

$$
\begin{aligned}
A &= -k_B T \ln \Theta(\mu, T, V,) + \mu N_a \\
S &= \frac{U - A}{T} \\
G &= A + PV \\
H &= U + PV,
\end{aligned}
$$ (4.3.16)

which are absolute properties that can be converted to excess properties with Equation 3.3.1.

CHAPTER 5

HYDROGEN ADSORPTION RESULTS

Currently, in the majority of reports of hydrogen adsorption into COFs, the data is obtained through the previously described simulation methods. As scarce as experimental data may be, there have been some studies reported. One such study reports the experimental data for COF-1, COF-5, COF-102, and COF-103 at 77 K as shown in Figure 5.1 in which the adsorption was measured with a gravimetric method [33]. Comparison of these results with that of simulations of adsorption of the same COFs (Figure 5.2a) performed by the same group[32] shows some discrepancies. The simulation overestimated the H_2 excess uptake for COF-1, COF-102, and COF-103. However it did provide an accurate estimation for COF-5. Differences between the simulated and experimental results are to be expected because of the previously described experimental issues present. The overestimation of the excess adsorption in this report may also cast doubt in the validity of the total gravimetric adsorption (Figure 5.2b) and the volumetric adsorption (Figure 5.3) [32]. All the same the results do suggest the possibility for COFs to be used as hydrogen storage materials. COF-105 and COF-108 have very high total gravimetric H_2 uptake well beyond the ultimate DOE goal which can be explained by their very low densities. Consequentially COF-105 and COF-108 have a lower total volumetric uptake than the other 3D COFs (COF-102 and COF-103), but all four are above the DOE 2015 goal.
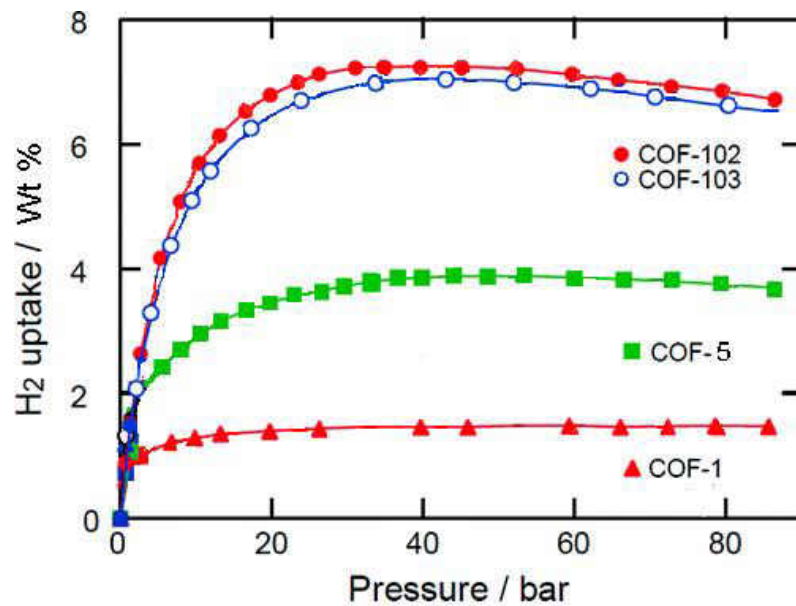
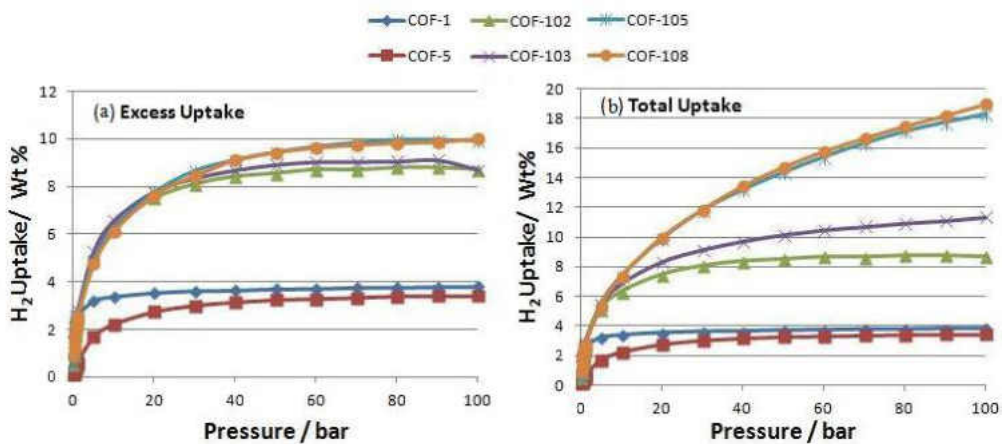Figure 5.1. Experimental excess H_2 adsorption at 77 K [33].

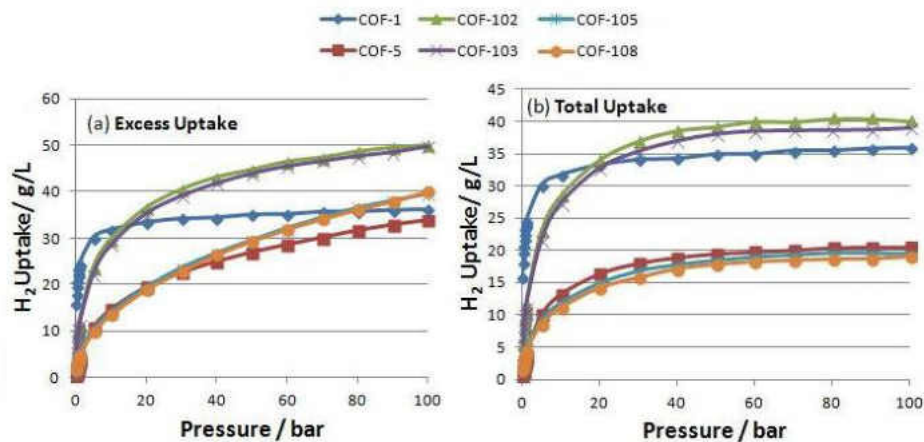Figure 5.2. Simulated excess (a) and absolute (b) H_2 adsorption at 77 K in gravimetric units [32].

Figure 5.3. Simulated excess (a) and absolute (b) H_2 adsorption at 77 k in volumetric units [32].

Simulations of hydrogen adsorption into COF-202 show that COF-202 is also above the DOE 2015 goal for both gravimetric and volumetric H_2 uptake (Figure 5.4a,b) [49]. These simulations were obtained with the previously described first-princibles based GCMC method. Simulations of H_2 adsorption into COF-202 were also performed at 298 K to coincide with the DOE requirement. Results from these simulations showed a dramatic decrease in both the gravimetric and volumetric uptake as shown in Figure 5.4c,d [49]. Large decreases in adsorption of other COFs were observed when performed at 298K [8]. Likewise, COF-300 and COF-301 were found to have poor H_2 uptake at 298 K (Figure 5.5) [50]. These results are not surprising because the binding energies between H_2 and the COF are too small for H_2 to be held at 298 K. If COFs are to be used as H_2 storage materials, modifications must be made to afford better adsorption at ambient temperatures.

5.1   Expanded Wang-Landau Simulations

In our EWL simulations [51], the adsorbtion of H_2 into COF-102, COF-105, and COF-108 was modeled with a Morse potential, Equation 4.2.1. The parameters for this
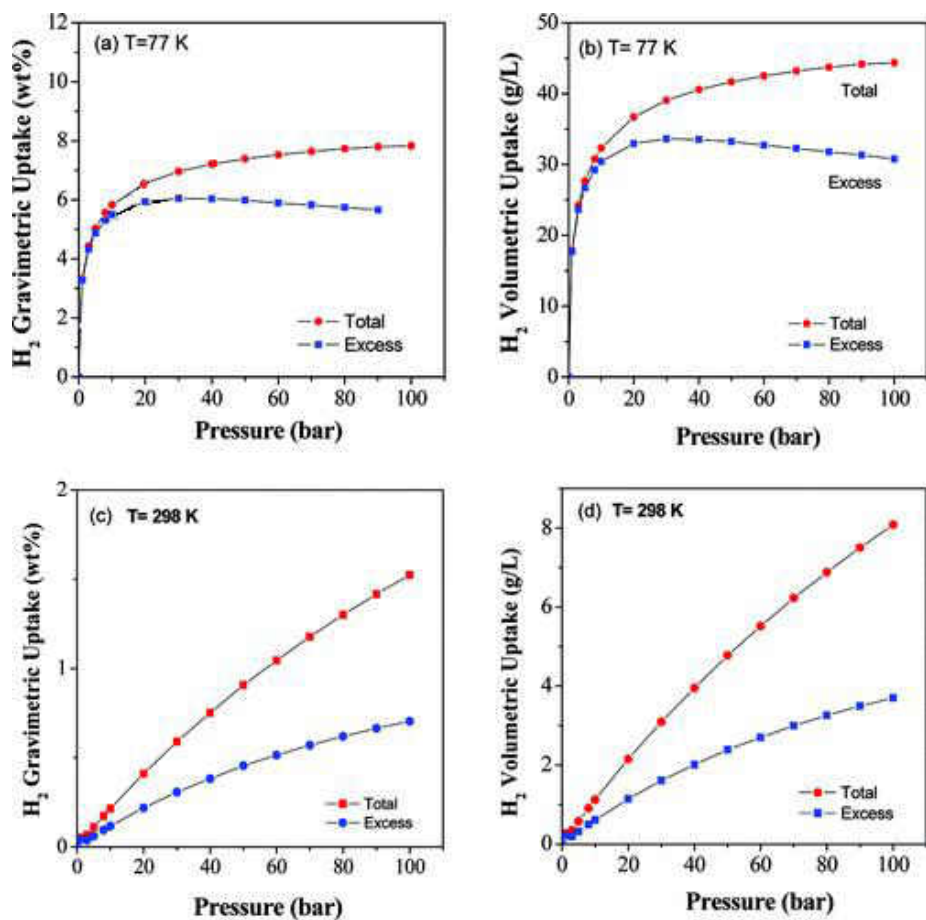
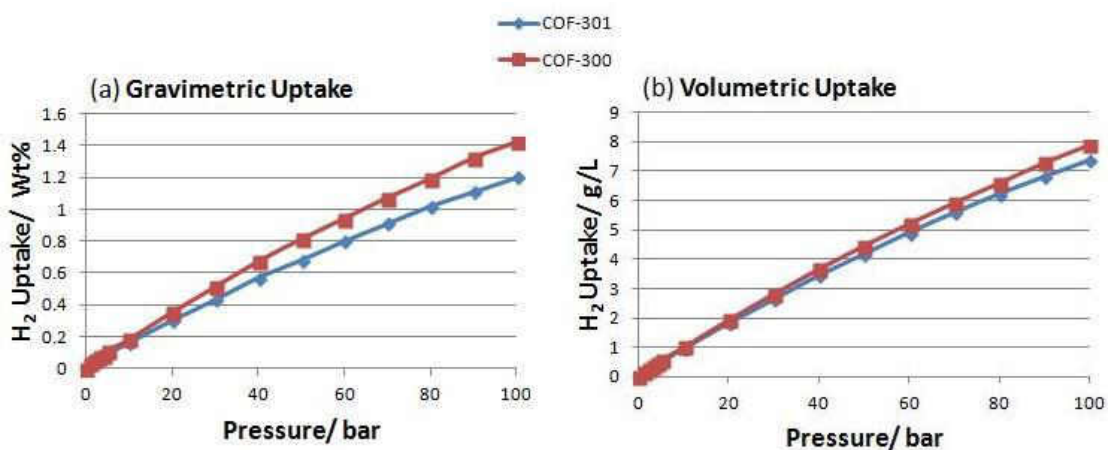Figure 5.4. Simulated H$_2$ adsorption of COF-202 at 77 K (a,b) and 298 K (c,d) [49].

Figure 5.5. Simulated total H$_2$ adsorption at 298 K in gravimetric (a) and volumetric (b) units [8].

Table 5.1. Force field parameters from Han *et al.* [32]

	D(kcal/mol)	$r_0(\mathring{A})$	α
C–H_A	0.10082	3.12022	12.00625
H–H_A	0.00087	3.24722	12.00625
H_A–H_A	0.01815	3.56980	10.70940
O–H_A	0.02515	3.32249	12.00187
B–H_A	0.04825	3.49300	10.56518
Si–H_A	0.11014	3.53350	14.16509

H_A denotes a hydrogen atom of a H_2 molecule

force field were obtained from accurate second order Møller-Plesset calculations done by Han *et al.* [32] and are displayed in Table 5.1. Bonded and nonbonded parameters for atoms of the COF itself is not needed because COFs are quite rigid, this allows the assumption of negligible compression of the COF structure, thus the coordinates of the atoms of the COF are to remain fixed throughout the simulation. One unit cell of each COF was used for the simulations and the cell parameters of each COF were acquired from [2] and are displayed in Table 5.2. There was also no need for bonded parameters for the hydrogen molecule since the bond length of the H_2 molecules was fixed at 0.74 $\mathring{A}$. Force field parameters for interactions with the partial molecule in stage l with $M = 100$ steps were scaled as follows: $D_{ij,\xi} = (l/M)^{1/3} D_{ij}$, $r_{0ij,\xi} = r_{0ij}/(l/M)^{1/2}$, and $0.74(l/M)^{1/4}$ for the bond length of a fractional H_2. Inputs for the EWL algorithm are as follows: the flatness criterion for the histogram required that each (N,l) be visited 1000 times, the starting convergence factor was $f = e$ and was reduced by a factor of $\sqrt{2}$, lastly, each step consists of either at translation of a H_2 molecule (37.5% of the steps), a rotation of a H_2 molecule (37.5% of the steps), or a change in (N,l) (25% of the steps). Simulations were performed at two temperatures, $T = 77$ K and $T = 298$ K for each COF and for bulk hydrogen which allows for the conversion of absolute to excess properties. Some results of the bulk H_2 simulation are given in Figure 5.6 and are in good agreement with experimental results [52].

Table 5.2. Cell parameters for COF-102, COF-105 and COF-108 [2]

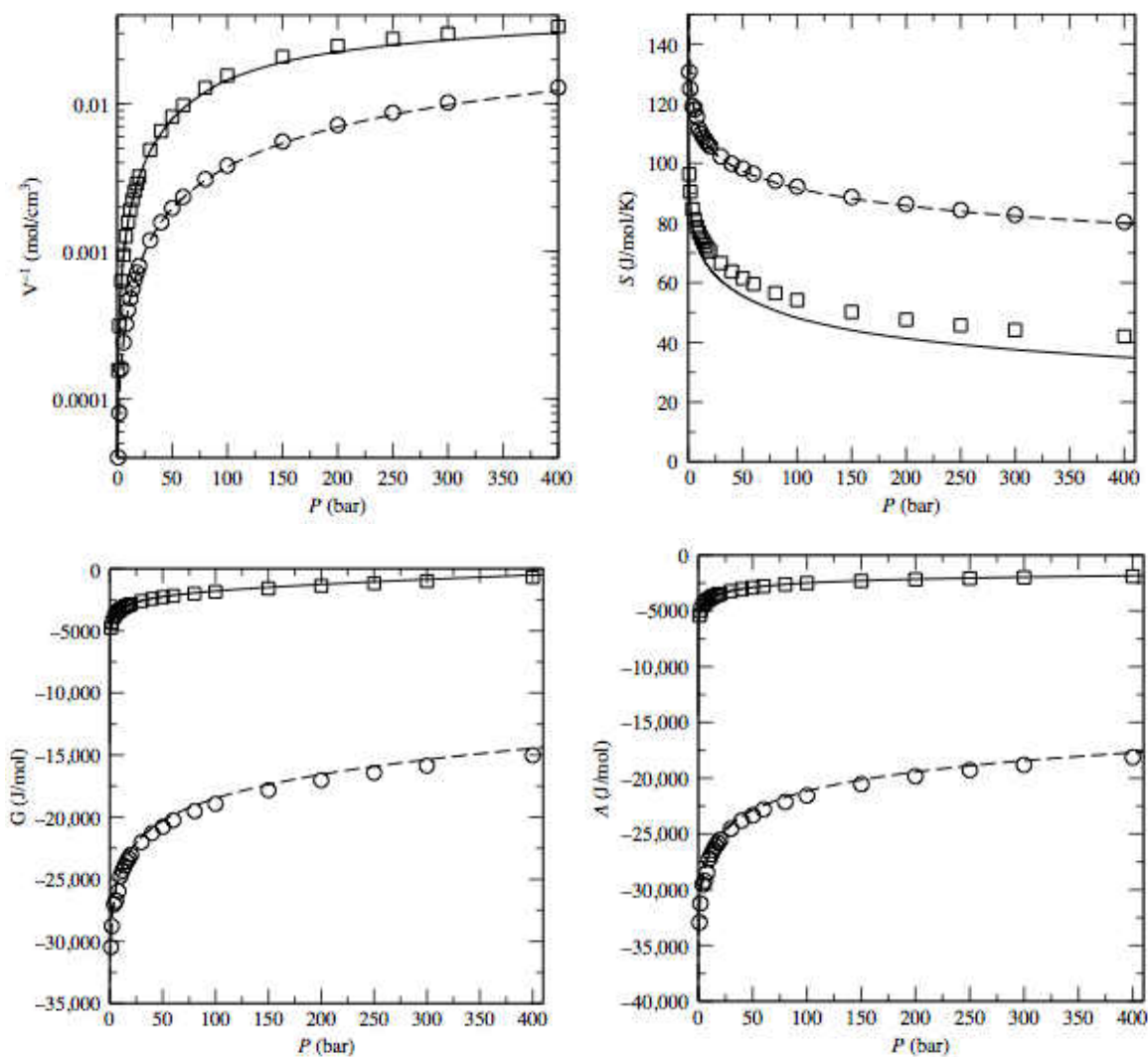|	COF-102	COF-105	COF-108
Space group symmetry	I43d	I4sd	P43m
a = b = c (Å)	27.177	44.886	28.401
Unit cell volume (Å^3)	20,073	90,434	22,909

Figure 5.6. Molar properties: volume (top left), entropy (top right), Gibbs free energy (bottom left), and Helmholtz free energy (bottom right) of Hydrogen from EWL simulations. Results at T = 77 K are shown with a solid line and with a dotted line at T = 298 K [51]. The open squares and circles are experimental data [52] at 77 K and 298 K respectively.

From the COF with H_2 EWL simulations, an accurate estimate for the grand canonical partition function was obtained which allows for the determination of the absolute amount of H_2 adsorbed at pressures up to 100 bar. The absolute adsorption isotherms at $T = 77$ K and $T = 298$ K for COF-102, COF-105, and COF-108 are shown in Figures 5.7–5.9, respectively. Snapshots of the cell with adsorbed hydrogen in the three COFs are shown in Figure 5.10. The open squares in these figures represent GCMC results from [32] and are in good agreement with experimental data. These results show a good agreement of GCMC and EWL simulations in the determination of H_2 adsorption isotherms. In Table 5.3 the gravimetric and volumetric capacity of hydrogen in the COFs and the DOE targets is shown. All three of the COFs at 77 K are well beyond the DOE's ultimate goal for gravimetric capacity, COF-108 being the greatest at 18.89 wt% and are near or above the 2015 volumetric target, COF-102 being the greatest at 50.87 g/L. As is expected a large decline in H_2 adsorption is observed at $T = 298$ K because of the decreased density of hydrogen and the weak H_2– COF interaction energy. This suggests that these COFs need to undergo some modification if they are to be used as storage materials at ambient conditions.

The Gibbs free energy, enthalpy, and entropy of the adsorbed hydrogen was also determined using Equation 4.3.16 for each COF at 77 K and 298 K. Then the Gibbs free energy, enthalpy, and entropy of immersion was determined using Equations 3.2.42 and 3.2.38. As expected, the enthalpy, entropy and Gibbs free energy of immersion are negative and thus for the opposite process (desorption) are all positive. The dependence from the these values with the pressure and implicitly the number of molecules adsorbed is shown in Figure 5.11. A logarithmic increase in the three state functions is seen at 77 K and begin to plateau at 100 bar. This is occurring because within the lower pressure range the difference between the adsorbed phase and the bulk phase is large. But as the pressure increases, the system is becoming

more and more saturated with hydrogen which causes the difference of the two phases to decrease. Much smaller values for the three state functions are observed at 298 K because the amount adsorbed was much less than that of the COFs at 77 K. Comparison of the state functions relative to the specific COF shows little difference which is not that unreasonable given the similarity of the three COFs. A comparison of the desorption Gibbs free energy of the COFs at both temperatures is given in Figure 5.12.
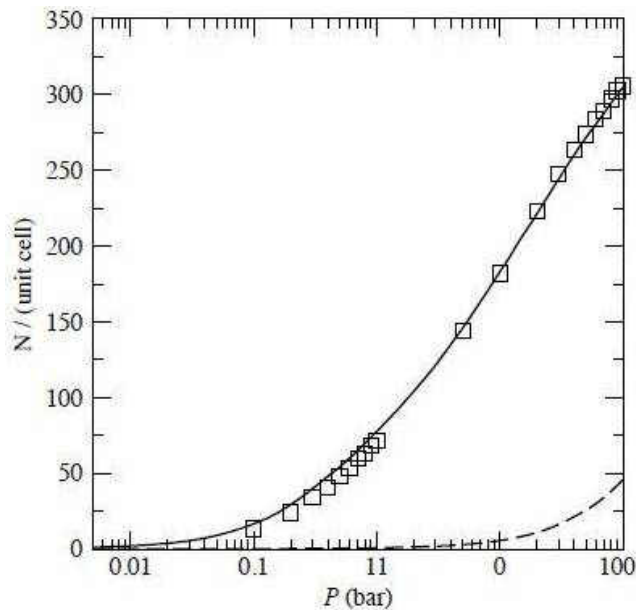

Figure 5.7.   Adsorption isotherm for H_2 in COF-102.   Solid line and dashed line represent the EWL results at $T = 77$ K and $T = 298$ K, respectively [51]. The open squares represent the GCMC results at $T = 77$ K from [32].

5.2   Improved Hydrogen Adsorption into COFs

The poor hydrogen adsorption performance of COFs at ambient temperatures has lead to much research to improve its H_2 storage ability. MOFs were previously found to be limited by this issue as well, which leads to the recommendation by Han and Goddard [53] to dope MOFs with electropositive metals. The intent of this recommendation
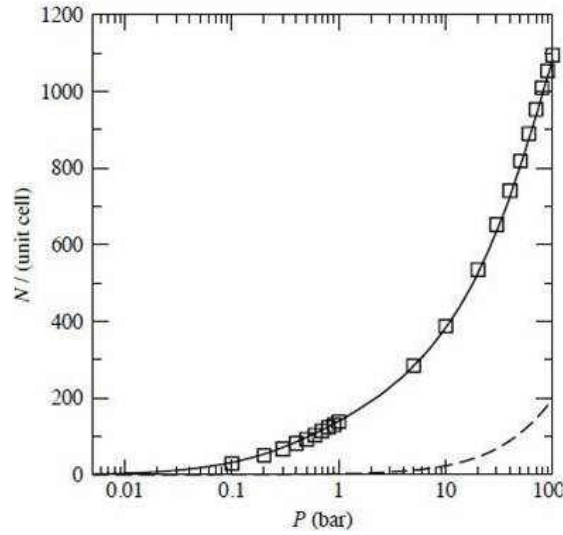
Figure 5.8. Adsorption isotherm for H_2 in COF-105. Solid line and dashed line represent the EWL results at $T = 77$ K and $T = 298$ K, respectively [51]. The open squares represent the GCMC results at $T = 77$ K from [32].

Figure 5.9. Adsorption isotherm for H_2 in COF-108. Solid line and dashed line represent the EWL results at $T = 77$ K and $T = 298$ K, respectively [51]. The open squares represent the GCMC results at $T = 77$ K from [32].
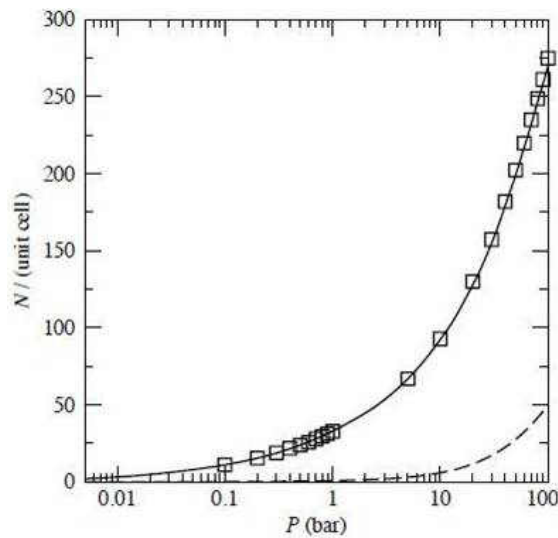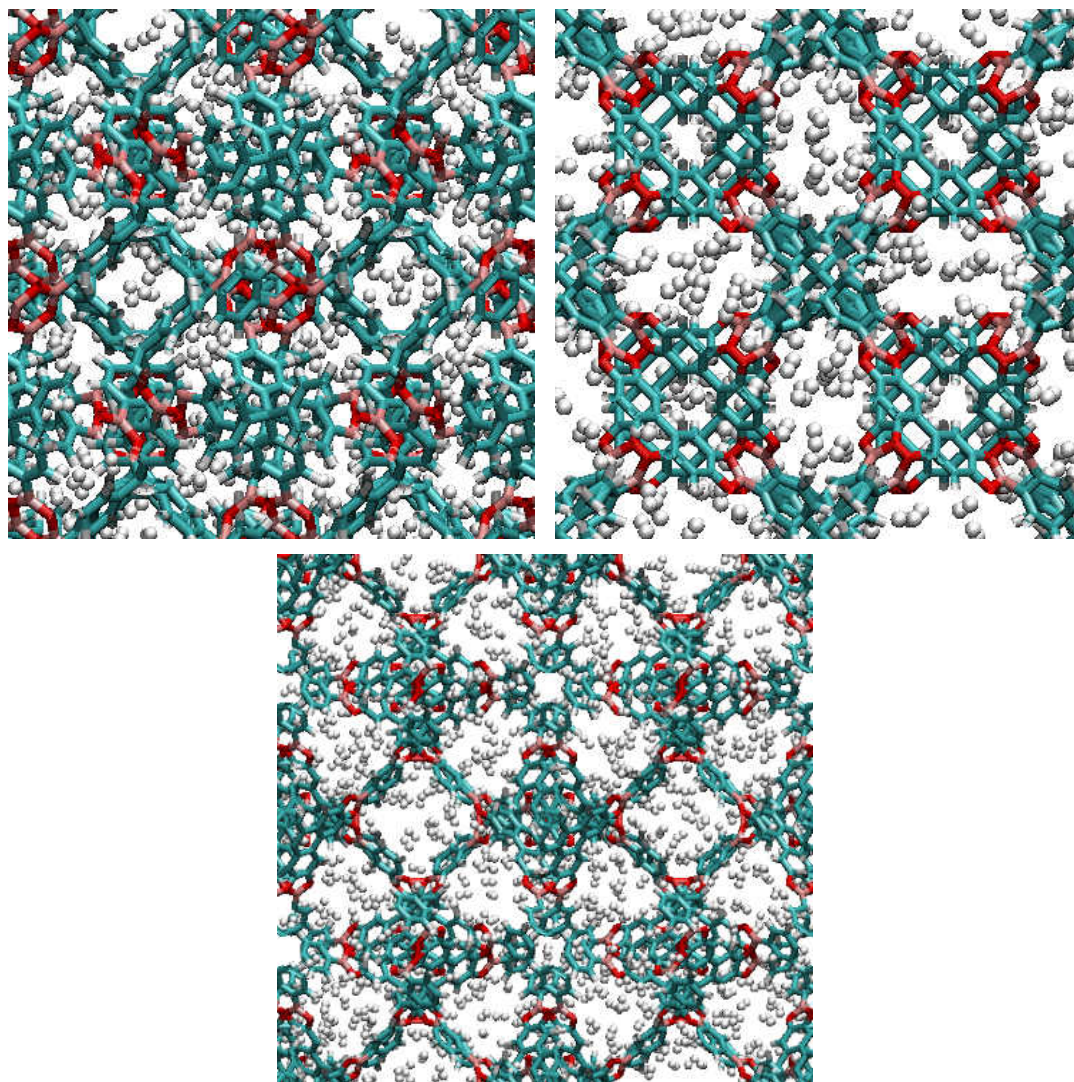
Figure 5.10. Snapshots for the adsorption of H_2 in COF-102 (top left), COF-105 (bottom), COF-108 (top right) [51].

Table 5.3. Hydrogen Capacity of COFs

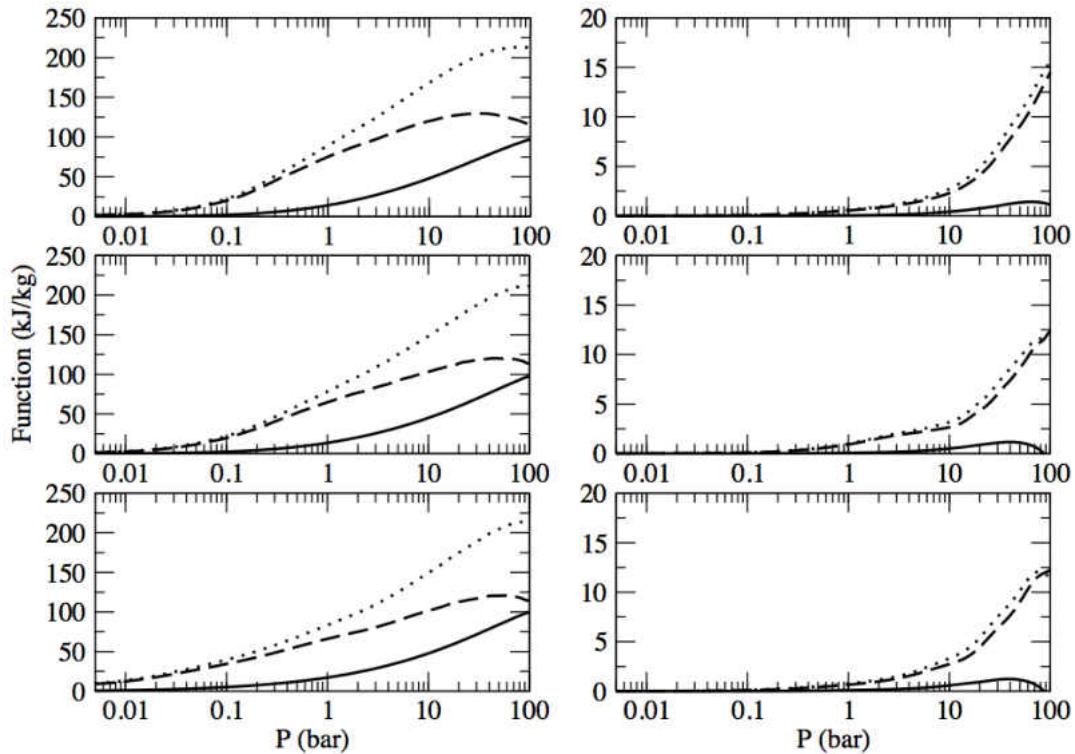|	Gravimetric (wt%)	Volumetric (g/L)
DOE 2015 Goal	5.5	40
DOE Ultimate Goal	7.5	70
COF-102 at 77 K	11.04	50.87
COF-105 at 77 K	18.27	40.24
COF-108 at 77 K	18.89	39.60
COF-102 at 298 K	1.84	7.67
COF-105 at 298 K	3.97	7.44
COF-108 at 298 K	4.12	7.31

Figure 5.11. Desorption functions (kJ/kg of COF) vs. pressure at 77 K (left panel) and at 298 K (right panel). On both panels results are shown for COF-102 (top), COF-105 (middle) and COF-108 (bottom). Gibbs free energy is shown with solid line, enthalpy with a dotted line and entropy multiplied by T with a dashed line [51].
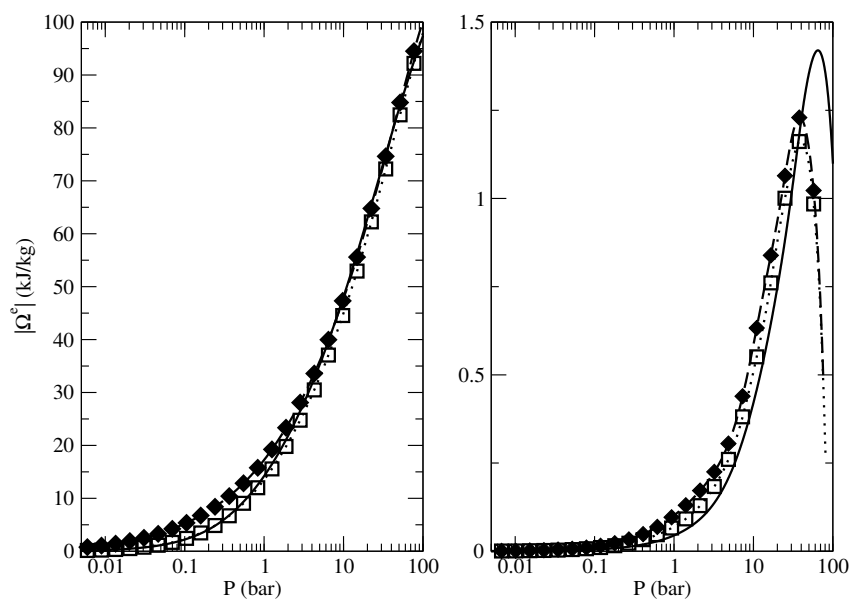
Figure 5.12. Desorption Gibbs free energy (kJ/kg of COF) against pressure at 77 K (left) and at 298 K (right). For both temperatures, COF-102 is shown with a solid line, COF-105 with open squares on a dotted line and COF-108 with filled diamonds on a dashed line [51].

was to increase the binding energies of H_2 with the framework to allow for greater adsorption at ambient temperatures. This recommendation has been shown to increase the H_2 capacity of MOFs and was therefore similarly applied to COFs. Lithium has been commonly used, but other alkaline metals [54] and also alkaline earth metals have been used [55, 56]. All the studies of metal doped COFs to the author's knowledge have been theoretical. Simulation methods, similar to undoped COFs, are used to create H_2 adsorption isotherms. The structures of the doped COFs are determined with DFT calculations, followed by first-principles based GCMC. From these simulations, a large improvement in H_2 adsorption at 298 K was reported for COF-102, COF-103, COF-105, and COF-108 (FIgure 5.13) [41]. Similar findings have been reported by others, but all of these are only theoretical and experimental data has yet to be obtained.

Another variation that has been experimented with is the metalation of imine linked COFs with palladium. The difference from metal doping is that in this process the metal is chemically bound to the framework as opposed to being simply adsorbed in it. In this process reported by Yaghi [57], $PdCl_2$ is refluxed with COF-301 in acetonitrile to yield the metalated product. First-principles based GCMC simulations at 298 K gave results that are high above the DOE 2015 goal for volumetric storage with a total volumetric uptake of 60 g L^{-1} but came up short of gravimetric target with 4.2 wt% [50]. Given these results, COF-301-$PdCl_2$ is the best H_2 storage material at 298 K to date.
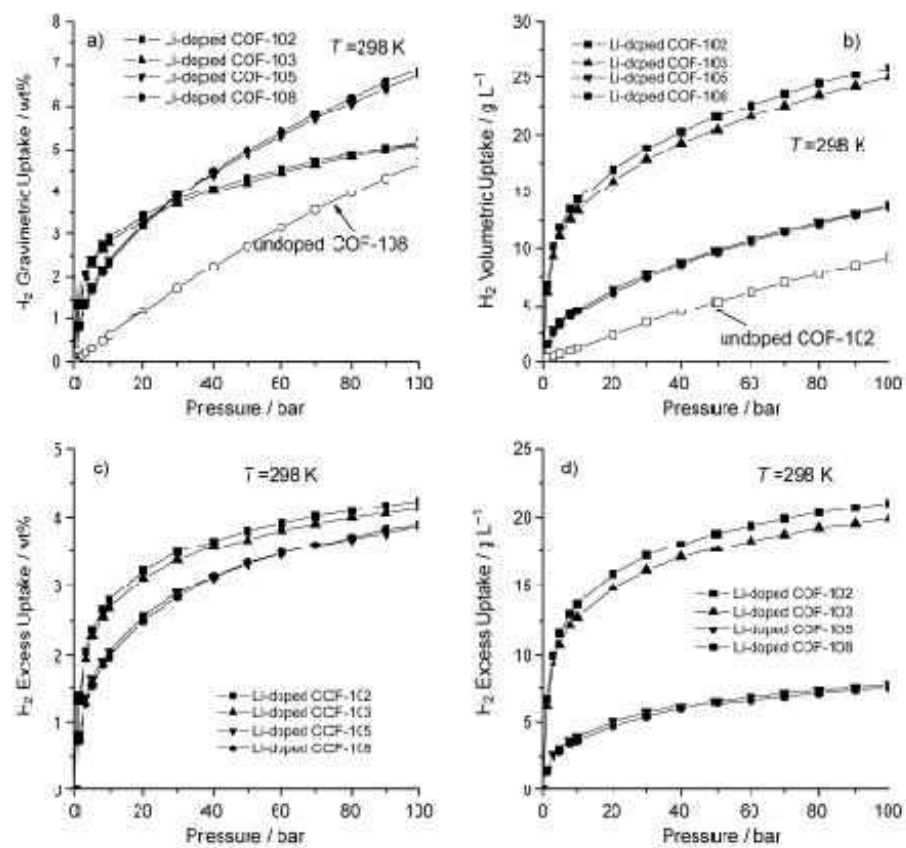
Figure 5.13. Simulated H$_2$ adsorption of Li-doped COFs at 298 K [41].

CHAPTER 6

MOLECULAR DYNAMICS

Molecular dynamics is a type of computer simulation that computes the movements of atoms and molecules. This is commonly performed by solving Newton's equations of motion with numerical methods. As previously described, a force field that models the interactions between atoms is used to determine the force acting on each atom, from which the velocities and positions can be calculated. This chapter describes how molecular dynamics are performed and provides example calculations of an argon system. This is followed with results from systems of pure hydrogen to show applicability of this method. Lastly simulations of hydrogen in COF molecules are performed to determine the diffusion coefficients which would be useful in determining the rate of hydrogen release from the COF storage system.

6.1   GROMACS

GROMACS (GROningen MAchine for Chemical Simulations) originally developed from the biophysical chemistry department of the University of Groningen, is a commonly used open source software package for molecular dynamics simulations. GROMACS was originally designed for simulations of proteins and other biological molecules. However, because of its compatibility with multiple force fields and extensive collection of built-in programs and simulation parameters, it can be used to perform simulations of many different systems.

The steps to perform a molecular dynamics simulation start with a structure file containing the Cartesian coordinates of the atoms and their connectivity. Also, the structure must be compatible with a force field accepted by GROMACS. The force field used in the molecular dynamics simulation consists of parameters that are unique to each combination of atoms. These parameters are then input into potential functions that model the bonded and non-bonded interactions. From there, GROMACS can create the desired system to be simulated (*e.g.*, number of molecules and simulation box size and shape). Following the creation of the simulation box, an energy minimization step is necessary to rearrange the molecules of the system to a stable configuration. GROMACS has a few different algorithms for energy minimization, one of which is steepest descent. The goal of this algorithm is find a local minimum in the force field functions of the system. This is accomplished by repositioning the atoms of the system in the direction of the steepest local gradient of the potential. The repositioning of the atoms must result in a decrease of the potential, otherwise the move is rejected and the maximum displacement constant is then scaled back to try a different configuration. Reposition of atoms continues until the number of specified iterations is met or all atoms are below the specified force threshold. The force felt by an atom is the negative gradient of the potential calculated from the force field. To simplify the calculation of the potential of each atom, the contributions from surrounding atoms is limited to those atoms within a user specified distance. The next step is to equilibrate the system in an NVT ensemble. At the start of this simulation, velocities $\boldsymbol{v}_i$ at a given temperature T are generated from the Maxwell–Boltzmann velocity distribution shown in Equation 6.1.1. The velocity assigned to each atom is determined by multiplying a scalar in the range of $-6 \leq a < 6$ times the standard deviation $\sqrt{kT/m_i}$ of Equation 6.1.1. The scalar is the sum minus 6 of twelve random numbers form zero to one.

$$p(\boldsymbol{v}_i) = \left(\frac{m_i}{2\pi kT}\right)^{\frac{1}{2}} \exp\left[-\frac{m_i \boldsymbol{v}_i^2}{2kT}\right] \qquad (6.1.1)$$

Once initial velocities are known, Newton's equations of motion can be solved with a specified algorithm to determine the new trajectories of the system. A leap-frog algorithm, similar to the velocity Verlet algorithm, calculates the position and midpoint velocities with a second order approximation. First, the new half step position $\boldsymbol{r}$(t+ $\frac{1}{2}$Δt) where Δt is given time step of the simulation and is on the order of 10^{-15}s is calculated from Equation 6.1.2.

$$\boldsymbol{r}(t + \frac{1}{2}\Delta t) = \boldsymbol{r}(t) + \frac{1}{2}\Delta t \boldsymbol{v}(t) + \frac{\Delta t^2}{4m}\boldsymbol{F}(t) \qquad (6.1.2)$$

The force, $\boldsymbol{F}(t)$, is acquired by taking the gradient of the potential functions from the force field for each atom at time t. Shifting the time coordinate a half time step changing $\boldsymbol{r}$(t + $\frac{1}{2}$Δt) to $\boldsymbol{r}$(t) thus changes the initial velocity to $\boldsymbol{v}$(t - $\frac{1}{2}$Δt) allowing the algorithm to continue with Equations 6.1.3 and 6.1.4 for the specified number of time steps.

$$\boldsymbol{v}(t + \frac{1}{2}\Delta t) = \boldsymbol{v}(t - \frac{1}{2}\Delta t) + \frac{\Delta t}{m}\boldsymbol{F}(t) \qquad (6.1.3)$$

$$\boldsymbol{r}(t + \Delta t) = \boldsymbol{r}(t) + \Delta t \boldsymbol{v}(t + \frac{1}{2}\Delta t) \qquad (6.1.4)$$

During the simulation, the temperature of the system is computed from the kinetic energy shown in Equations 6.1.5 and 6.1.6. In order to hold the temperature of the system constant during the leap-frog iterations, a temperature coupling algorithm must be used. This can be done with the Berendsen algorithm [58], Equation 6.1.7, with time constant, τ, which is analogous to the system placed in an external water bath at constant temperature T_0. Another temperature coupling algorithm is

velocity-rescaling coupling [59] shown in Equation 6.1.8 where $\overline{K}$ is the desired kinetic energy, τ is the coupling constant, N_f is the number of degrees of freedom, and dW is a first order Wiener process (a continuous-time Markov process). This coupling method is advantageous because the term on the left results in first order decay in temperature deviations and the term on the right allows for the correct kinetic energy distribution for the canonical ensemble.

$$E_{kin} = \frac{1}{2} \sum_{i=1}^{N} m_i v_i^2 \tag{6.1.5}$$

$$\frac{1}{2} N_{df} kT = E_{kin} \tag{6.1.6}$$

$$\frac{dT}{dt} = \frac{T_0 - T}{\tau} \tag{6.1.7}$$

$$dK = (\overline{K} - K)\frac{dt}{\tau} + 2\sqrt{\frac{K\overline{K}}{N_f}} \frac{dW}{\sqrt{\tau}} \tag{6.1.8}$$

The final step in the equilibration process is to perform a molecular dynamics simulation in an NPT ensemble to set the system at a specified pressure by scaling the simulation box vectors. The Berendsen algorithm can be used to hold the system to the desired pressure by replacing the temperature terms in Equation 6.1.7 with pressure terms. A more accurate to the NPT ensemble pressure coupling is the Parrinello-Rahman coupling [60], which is shown in Equation 6.1.9, where matrix $\mathbf{W}^{-1}$ determines the strength of coupling with the parameters β, the compressibilities, τ_P, the pressure time constant and L, the largest box length. Following these preparatory simulations, the system is ready to run more extensive molecular dynamics simulations.

$$\frac{db^2}{dt^2} = V\mathbf{W}^{-1}\mathbf{b}'^{-1}(\mathbf{P} - \mathbf{P}_{\text{ref}})$$

$$(6.1.9)$$

$$(\mathbf{W}^{-1})_{i,j} = \frac{4\pi^2\beta_{i,j}}{3\tau_P^2 L}$$

6.2 Argon Simulations

An argon system was used to demonstrate the phase change modeling capabilities of molecular dynamics simulations with GROMACS. A simulation box with 100 argon atoms, parameters of the force field for the argon system and a procedure for a phase change simulation was used from a tutorial for GROMACS [61]. First, a molecular dynamics run was performed using the leap-frog algorithm with a 2 femtosecond time step for 500,000 steps in an NVT ensemble where the temperature was held at 100 K with Berendsen temperature coupling. Since the boiling point of argon is 87.3 K, the system must be cooled to observe a phase change, this is done using the simulated annealing run parameter. Simulated annealing linearly changes the reference temperature used by the temperature coupling algorithm throughout a specified time range of the simulation. Following the simulated annealing molecular dynamics run of the argon system, the temperature at which a phase change occurred can be determined from the plots shown in Figure 6.1. A steep change in potential energy signals the occurrence of a phase change and comparison with the temperature plot yields the temperature at which the phase change occurred. The results of these simulations gave a much lower value (28 K) for the boiling point of argon compared to the literature value of 87.3 K. One way to improve this approximation is to decrease the rate of temperature change of annealing, which was found to improve the estimate of the boiling point to 55 K. The complete results of this modification is shown in Table 6.1.

The melting point of argon was also approximated with a similar technique. A
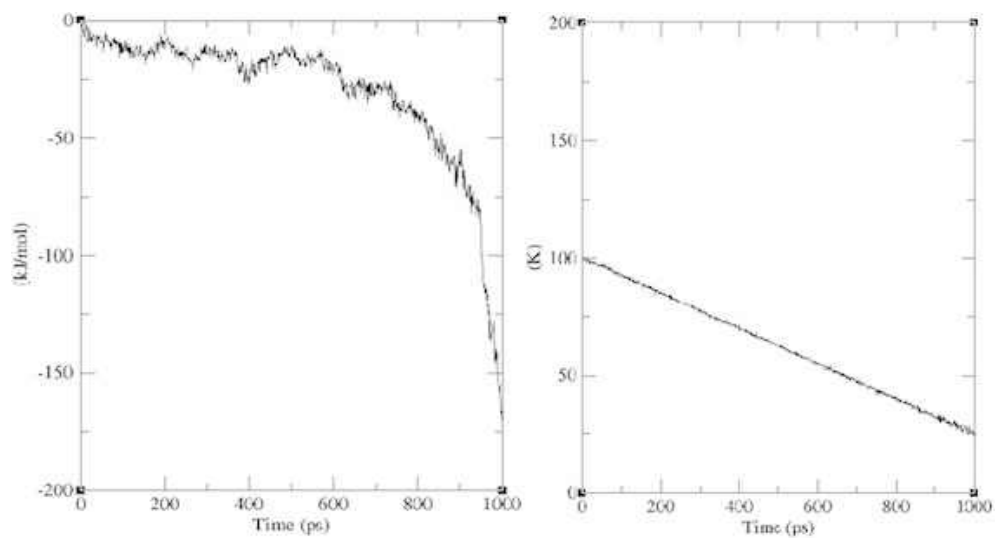
Figure 6.1. Condensation of Argon: (Left) Potential energy over time, (Right) Temperature over time.

Table 6.1. Boiling Point Approximations with Rate of Temperature Change

ΔT (K/fs)	Boiling Point (K)
7.5 x10^{-5}	28
1.5 x10^{-5}	45
7.5 x10^{-6}	48
3.75 x10^{-6}	50
3.75 x10^{-7}	55

simulation box of 216 argon atoms at a pressure of 10 bar and temperature of 100 K was cooled over 500,000 steps with a 2 femtosecond time step using simulated annealing to 0 K. From this simulation, the melting point was estimated to be 50 K, which is well below the literature value of 83.8 K, but could be improved by decreasing the rate of temperature change as seen in the boiling point estimation. The self-diffusion coefficient of argon was also calculated from linear regression of the mean square displacement of the atoms during the liquid phase of this simulation. The diffusion coefficient is one-sixth the slope of the mean square displacement given by the Einstein relation 6.2.1. The diffusion coefficient of argon was calculated to be 2.5 ± 0.3 x10^{-5} cm^{2}s^{-1} which is in agreement within uncertainties of the experimental value of 2.43 x10^5 cm^{2}s^{-1}.

$$\langle \| \boldsymbol{r}_i(t) - \boldsymbol{r}_i(0) \|^2 \rangle = 6Dt \qquad (6.2.1)$$

6.3   Molecular Dynamics Simulations of Hydrogen

The vapor liquid equilibrium properties of hydrogen was determined from molecular dynamics simulations with the software GROMACS using a procedure similar to that used for the previously described argon simulations. These simulations will serve as a way to determine an appropriate potential for hydrogen to be used for adsorption into COF simulations.

6.3.1   Simulation Setup

The force field used in the molecular dynamics simulation of hydrogen consists of bonded interactions and van der Waals forces. The Lennard-Jones potential, Equation 4.2.2, was used to model the van der Waals forces. Initiailly, Lennard-Jones parameters ($\varepsilon_{i,j} = 0.125520$ kJ mol^{-1}, $\sigma_{i,j} = 0.250000$) nm from the OPLS-AA force

field [62] for an alkane hydrogen was used in the simulations. Experimentation with literature values for Lennard-Jones parameters of hydrogen hydrogen interactions ($\varepsilon_{i,j}$ = 0.3063 kJ mol^{-1}, $\sigma_{i,j}$ = 0.2928 nm) [63] resulted in much poorer approximations, therefore the OPLS-AA parameters were used for the simulations. The bonded interactions were modeled as harmonic oscillators with Equation 6.3.1 derived from Hooke's law where the force constant $k_{i,j}$ = 331210.0 kJ mol^{-1} nm^{-2} [64] and the equilibrium bond distance $b_{i,j}$ = 0.07414 nm [65].

$$V(r_{ij}) = \frac{1}{2}k_{ij}(r_{ij} - b_{ij})^2 \tag{6.3.1}$$

A simulation box with 200 hydrogen molecules was generated with GROMACS and was followed with an energy minimization run using the steepest decent algorithm and a force tolerance of 10 kJ mol^{-1} nm^{-1}. A molecular dynamics run in the NVT ensemble was done to equilibrate the system at 41 K followed by a run in the NPT ensemble to obtain the desired pressure. Simulated annealing molecular dynamics simulations similar to those previously described for the argon system were performed to determine the boiling points of hydrogen at pressures ranging from 1–13 bar.

6.3.2   Results

From the procedure described above, a vapor pressure plot, vapor liquid equilibria data and the self diffusion coefficient of hydrogen was obtained. The boiling point of hydrogen at 1 bar from the simulation was determined to be 19.1 K which is comparable to the experimental value of 20.3 K. The potential energy and temperature plots from this simulation are shown in Figure 6.2. Agreement between simulation and experimental results [66] is observed in the pressure range of 1 − 5 bar, beyond 5 bar the simulation overestimates the boiling point as seen in the vapor pressure plot (Figure 6.3). The relationship between vapor pressure and temperature can be

modeled with the Antoine equation shown in Equation 6.3.2.

$$\log_{10} p = A - \frac{B}{C + T} \tag{6.3.2}$$

The coefficients of the Antoine equation for both the experimental [67] and simulated data are shown in Table 6.2. As seen in Figure 6.3, the Antoine relation holds for the experimental data throughout the pressure range, but deviates from simulated data points at higher pressures.
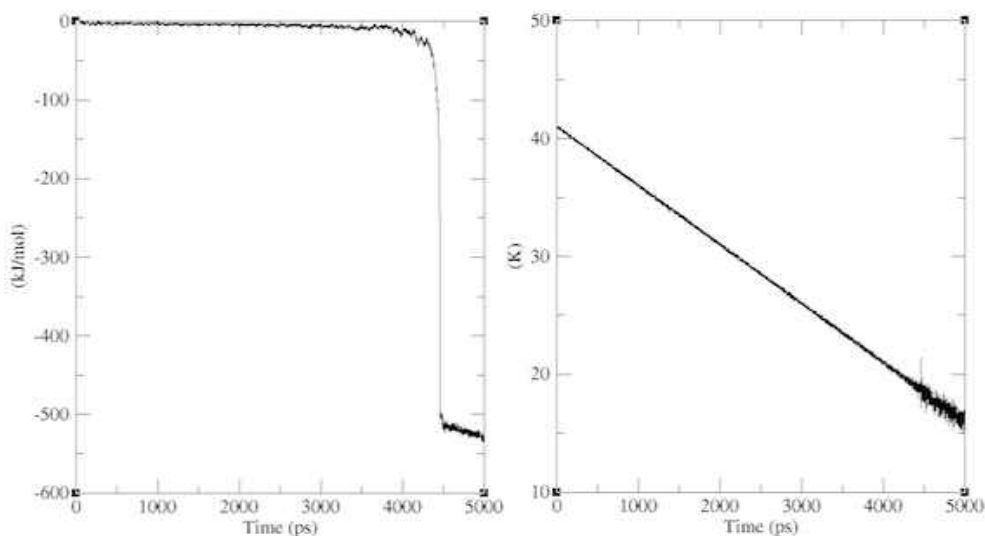

Figure 6.2. Potential energy plot and temperature plot of condensation of H_2 at 1 bar.

Table 6.2. Antoine Coefficients

	A	B	C
Experimental	3.543	99.395	7.726
Simulation	1.968	30.809	-3.397

A vapor-liquid coexistence curve was constructed with the experimental and simulated data to determine the critical properties of hydrogen (Figure 6.4). The critical temperature and density are determined by extrapolating the data with the scaling
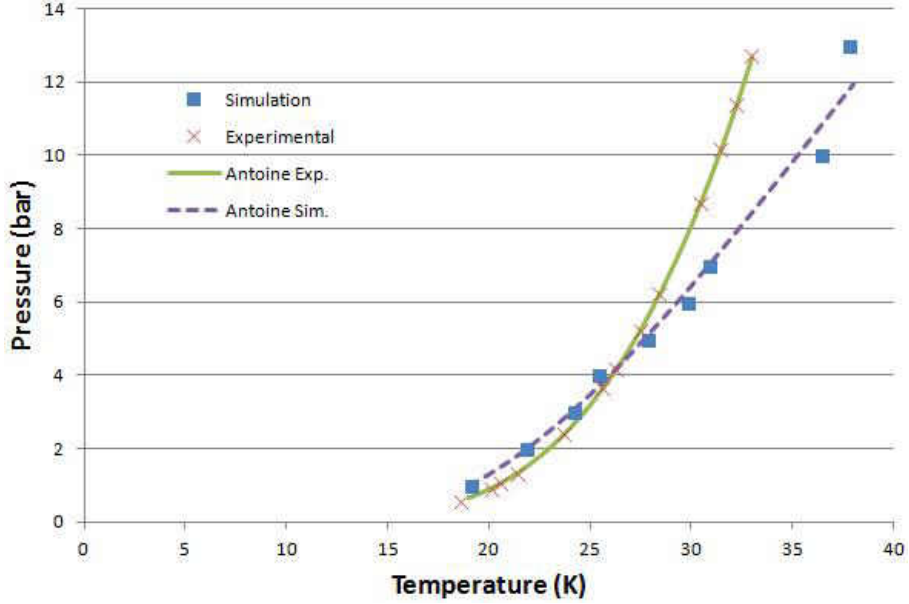
Figure 6.3. Vapor Pressure of H_2.

law and the rectilinear diameter law, Equations 6.3.3 and 6.3.4 respectively. The critical pressure can be calculated from Equation 6.3.2 once the critical temperature is known. The values of the constants of Equations 6.3.3, 6.3.4 and the critical properties are displayed in Table 6.3.

$$\rho_l - \rho_v = B \left(1 - \frac{T}{T_c} \right)^{\beta} \tag{6.3.3}$$

$$\frac{\rho_l + \rho_v}{2} = \rho_c + A \left(1 - \frac{T}{T_c} \right) \tag{6.3.4}$$

Lastly, the self-diffusion coefficient of hydrogen was determined from the Einstein relation. The diffusion coefficient at 15 K 1 bar from simulations was 0.61 ± 0.06 x10^{-6} cm^{-2} s^{-1} which is much smaller than the literature value of 0.4 x10^{-4} cm^{-2} s^{-1} [68, 69]. The large discrepancy may be accounted for by the density of liquid hydrogen from the simulations being about twice as large as the literature value. Since the simulation and experimental vapor densities are in agreement, the diffusion
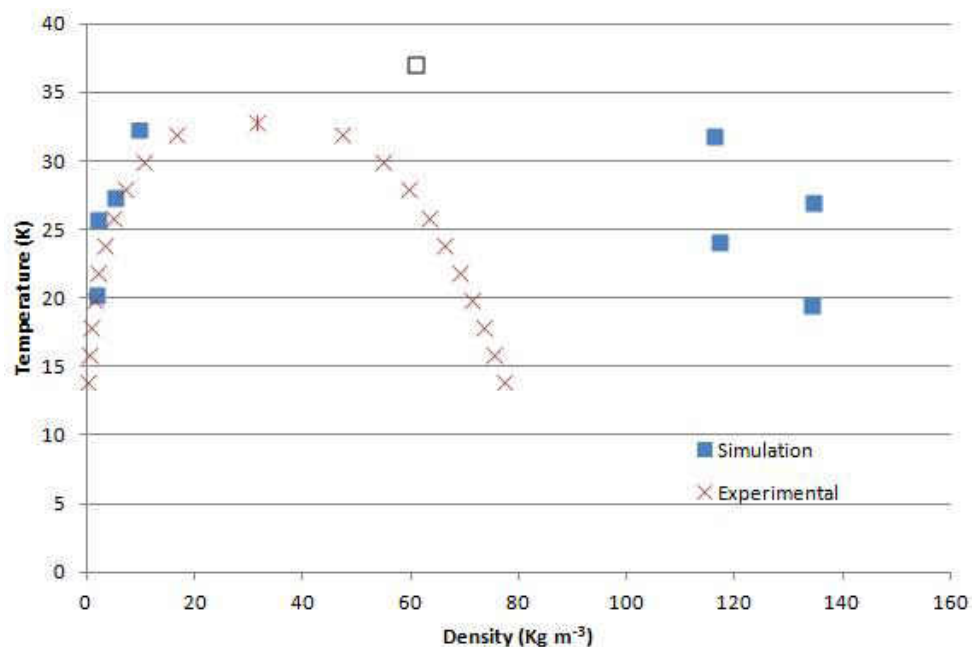
69

Figure 6.4. Vapor-liquid equilibria of H_2. The asterisk and open square mark the critical points determined form Equations 6.3.3,6.3.4.

coefficient was also calculated at 298 K 1 bar, which resulted in a slight difference in values between the simulation and experiment, 0.69010 ± 0.04260 cm^{-2} s^{-1} and 0.61 cm^{-2} s^{-1} [70], respectively.

Given from the results of the hydrogen molecular dynamic simulations, the use of the Lennard-Jones potential and harmonic bonding potential as the force field for molecular hydrogen simulations does fit with experimental results within a pressure range of 1 to 5 bar. However, re-parameterization of this force field is necessary for simulations beyond 5 bar.

Table 6.3. Critical Properties of Hydrogen

	B (kg m^{-3})	β	A (kg m^{-3})	T_c (K)	P_c (bar)	ρ_c (kg m^{-3})
Simulation	147.4	0.15931	12.048	37.09	11.31	61.03
Experiment	91.600	0.29288	12.374	32.85	12.40	31.41
*	-	-	-	32.97	12.93	31.02

*CRC Handbook of Chemistry and Physics

6.3.3 Diffusion of Hydrogen in the COFs

This section describes how the diffusion coefficients of H_2 in COF-102, COF-105, and COF-108 were determined using molecular dynamics simulations. Knowledge of the diffusion coefficients is of value because they are used in the calculation of loading and unloading times of H_2 into and out of COFs. The simulation box consists of one unit cell of the COF (a 2x2 unit cell was used for COF-108) and the corresponding number of H_2 molecules for each COF at $T = 77$ K, $P = 100$ bar from the previously described EWL simulations. A simulation of bulk H_2 at $T = 77$ K, $P = 100$ bar was also performed to be compared with the results of H_2 in the COFs. The force field parameters used in the EWL was also used for the MD simulations, but the Lennard-Jones potential model was used instead. The COFs were held rigid as with the EWL simulations, but vibrational motion in H_2 was allowed and was modeled as a harmonic oscillator given by Equation 6.3.1 where the force constant $k_{ij} = 331210$ kJ mol^{-1} nm^{-2} and the equilibrium bond length $b_{ij} = 0.07414$ nm.

The simulation box was first equilibrated at $T = 77$ K, $P = 100$ bar in the manner described in the previous section. Following equilibration, production md was run over a 4 ns period using a 1.7 nm neighbor search radius, velocity-rescaling and Parrinello-Rahman temperature and pressure coupling.

From these MD simulations, the mean square displacement (MSD) of the hydrogen molecules in each of the COFs is obtained. The diffusion coefficient D can then be calculated as one-sixth of the slope of the MSD curve given by the Einstein relation. The MSD curves of H_2 in each COF are shown in Figures 6.5–6.7 and the diffusion coefficients are displayed in Table 6.4.

From these results we find that the H_2 in COF-108 has the greatest diffusion coefficient of the other COFs at $D = 2.2747$ x10^{-4} cm^{2}s^{-1}, about half the value of bulk H_2 and four times that of COF-102. The fact that the relative order of the diffusion coefficients of the three COFs corresponds with the order of the pore volume

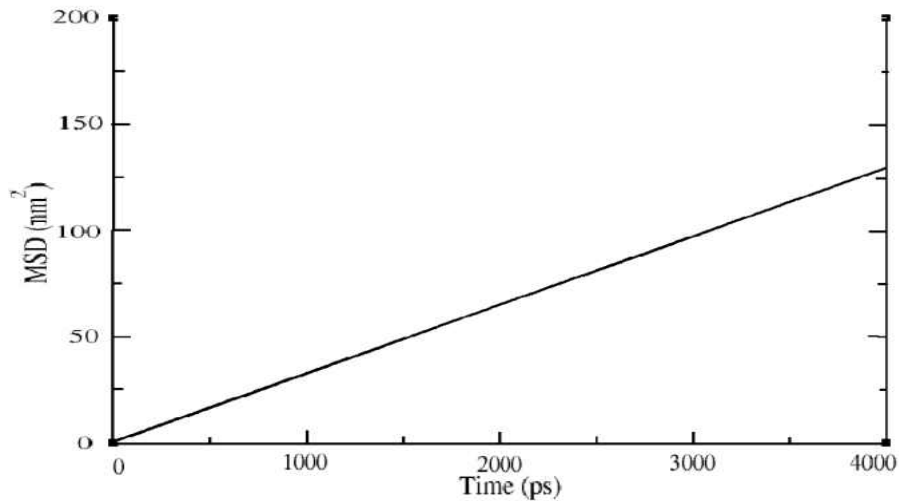offers some assurance in the validity of our results.

Figure 6.5. Mean square displacement of H_2 in COF-102 at $T = 77$ K, $P = 100$ bar over 4 ns.

Table 6.4. Diffusion Coefficients of H_2 in COFs at 77 K 100 bar

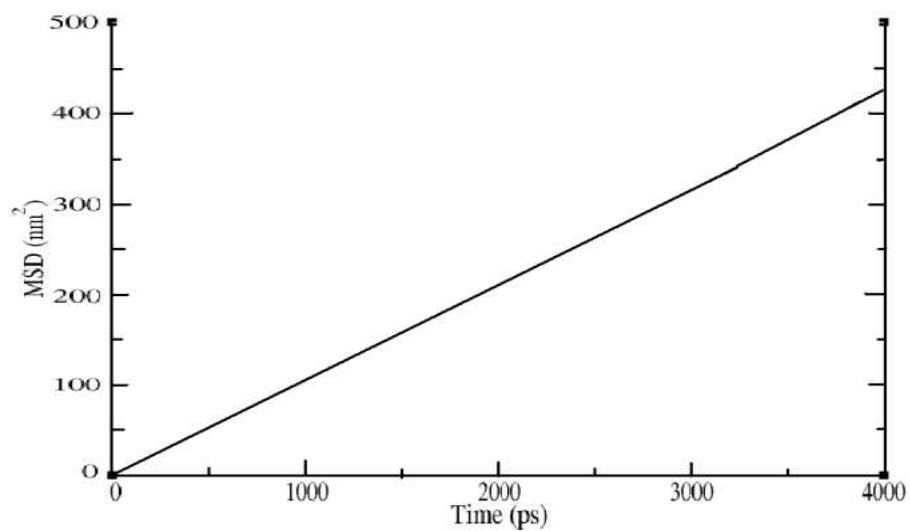|	D x10^{-5} cm^{2}s^{-1}
Bulk H_2 298 K 1 bar	61000*
Bulk H_2 298 K 1 bar	69000 $\pm$ 4000
Bulk H_2	46.74 $\pm$ 0.06
COF-102	5.66 $\pm$ 0.01
COF-105	17.92 $\pm$ 0.07
COF-108	22.7 $\pm$ 0.2

*Experimental data from [70]

Figure 6.6. Mean square displacement of H_2 in COF-105 at $T = 77$ K, $P = 100$ bar over 4 ns.
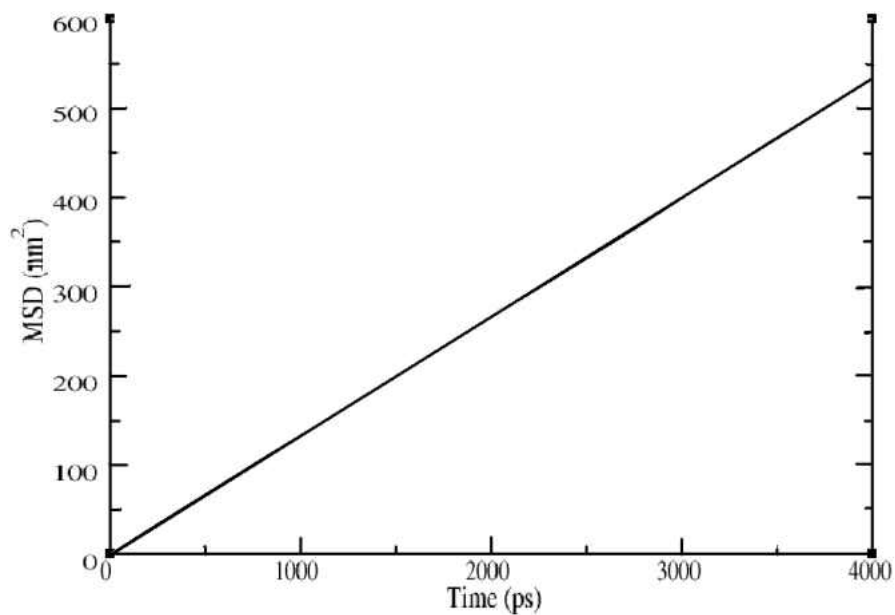

Figure 6.7. Mean square displacement of H_2 in COF-108 at $T = 77$ K, $P = 100$ bar over 4 ns.

CHAPTER 7

CONCLUSION

In summary, COFs have demonstrated to be a plausible material to be used in hydrogen storage applications. Relatively high quantities of hydrogen adsorbed into COFs compared to other storage methods have been reported. However, the lack of experimental data does draw some skepticism. Also, the theoretical data is typically an overestimate when compared to the limited experimental results and the best performing COF in favorable adsorption conditions (77 K) is not much higher than the DOE 2015 volumetric goal and this also does not consider the size of the actual storage system or the total deliverable quantity of hydrogen. Total deliverable H_2 needs to account for release of hydrogen at a sufficient rate to sustain combustion. On top of that, the performance of COFs at ambient temperatures is very poor, which has shown the need for modifications to the COF. From this observation, current work is focused primarily on the use of metal doping to improve hydrogen adsorption at ambient temperatures. Results from these works has shown large improvement in H_2 adsorption capacities at ambient temperatures and are also approaching the DOE 2015 goals. However, more research is needed, as these works are still in theoretical stages as metal doped COFs have yet to be synthesized. Nonetheless, COFs have drawn much excitement as a result of their potential application as hydrogen storage materials as well as their other possible applications, some of which have yet to be explored.

BIBLIOGRAPHY

[1] Côté, A. P.; Benin, A. I.; Ockwig, N. W.; O'Keffe, M. Matzger, A. J.; Yaghi, O. M. Porous, Crystalline, Covalent Organic Frameworks. *Science*, **2005**, *310*, 1166–1170.

[2] El-Kaderi, H. M.; Hunt, J. R.; Mendoza-Cortés, J.; Côté, A. P.; Taylor,, R. E.; O'Keeffe, M.; Yaghi, O. M. Designed Synthesis of 3D Covalent Organic Frameworks. *Science*, **2007**, *316*, 268–272.

[3] Yaghi, O. M.; O'Keeffe, M.; Ockwig, N. W.; Chae, H. K.; Eddaoudi, M.; Kim, L. *Nature*, **2003**, *423*, 705–715.

[4] Uribe-Romo, F. J.; Doonan, C. J.; Furukawa, H.; Oisaki, K.; Yaghi, O. M. Crystalline Covalent Organic Frameworks with Hydrazone Linkages. *J. Am. Chem. Soc.*, **2011**, *133*, 11478–11481.

[5] Côté, A. P.; El-Kaderi, H. M.; Furukawa, H.; Hunt, J. R.; Yaghi, O. M. Reticular Synthesis of Microporous and Mesoporous 2D Covalent Organic Frameworks. *J. Am. Chem. Soc.*, **2007**, *129*, 12914–12915.

[6] Hunt, J. R.; Doonan, C. J.; LeVangie, J. D.; Côté, A. P.; Yaghi, O. M. Reticular Synthesis of Covalent Organic Borosilicate Frameworks. *J. Am. Chem. Soc.*, **2008**, *130*, 11872–11873.

[7] Uribe-Romo, F. J.; Hunt, J. R.; Furukawa, H.; Klöck, C.; O'Keeffe, M.; Yaghi, O.M. A Crystalline Imine-Linked 3-D Porous Covalent Organic Framework. *J. Am. Chem. Soc.*, **2009**, *131*, 4570–4571

[8] Assfour, B.; Seifer, G. Adsorption of Hydrogen in Covalent Organic Frameworks: Comparison of Simulations and Experiments. *Microporous and Mesoporous Mat.*, **2010**, *133*, 59–65.

[9] Ding, S.; Gao. J.; Wang, Q.; Zhang, Y.; Song, W.; Su. C.; Wang, W. Construction of Covalent Organic Framework for Catalysis: Pd/COF-LZU1 in Suzuki–Miyaura Coupling Reaction. *J. Am. Chem. Soc.*, **2011**, *133*, 19816–19822.

[10] Wan, S.; Guo, J.; Kim, J.; Ihee, H. Jiang, D. A Belt-Shaped, Blue Luminescent, and Semiconducting Covalent Organic Framework. *Angew. Chem. Int. Ed.*, **2008**, *47*, 8826–8830.

[11] Wan, S.; Guo, J.; Kim, J.; Ihee, H. Jiang, D. A Photoconductive Covalent Organic Framework: Self-Condensed Arene Cubes Composed of Eclipsed 2D

Polypyrene Sheets for Photocurrent Generation. *Angew. Chem. Int. Ed.*, **2009**, *48*, 5439–5442.

[12] Keskin, S. Adsorption, Diffusion, and Separation of CH4/H2 Mixtures in Covalent Organic Frameworks: Molecular Simulations and Theoretical Predictions. *J. Phys. Chem. C.*, **2012**, *116*, 1772–1779.

[13] U.S. Department of Energy. Hydrogen Storage. http://www1.eere.energy.gov/hydrogenandfuelcells/storage/current_technology.html.

[14] Murray, L. J.; Dincă, M.; Long, J. R. Hydrogen storage in metal–organic frameworks. *Chem. Soc. Rev.*, **2009**, *38*, 1294–1314.

[15] Brunauer, S.; Deming, L. S.; Deming, W. E.; Teller, E. J. On a Theory of the van der Waals Adsorption of Gases. *J. Amer. Chem. Soc.*, **1940**, *62*, 1723–1732.

[16] Langmuir, I. Chemical Reactions at Low Pressures. *J. Amer. Chem. Soc.*, **1915**, *37*, 1139.

[17] Brunauer, S.; Emmett, P.H.; Teller, E. Adsorption of Gases in Multimolecular Layers. *J. Amer. Chem. Soc.*, **1938**, *60*, 309–319.

[18] Gregg, S. J.; Sing, K. S. *Adsorption, Surface Area and Porosity*, Academic Press: London, 1967; pp 93–103.

[19] Young, D. M.; Crowell, A. D. *Physical Adsorption of Gases*, Butterworths: Washington, 1962; pp 147–156.

[20] Ruthven, D. M. *Principles of Adsorption and Adsorption Processes*, Wiley: New York, 1984; 62–70.

[21] Yang, R. T. *Gas Separation by Adsorption Process*, Butterworths: London, 1987; 29–39.

[22] Suzuki, M. *Adsorption Engineering*, Elsevier: New York 1990.

[23] Hill, T. L. Theory of Physical Adsorption. *Adv. Catal.*, **1952**, *4*, 211–258.

[24] Shen, D.; Bülow, M.; Siperstein, F.; Engelhard, M.; Myers, A. L. Comparison of Experimental Techniques for Measuring Isosteric Heat of Adsorption. *Adsorption*, **2000**, *6* 275–286.

[25] Myers, A. L. Ch 21 of *Chemical Thermodynamics for Industry*, Royal Society of Chemistry: Cambridge, 2004.

[26] Myers, A. L. Equation of State for Adsorption of Gases and Their Mixtures in Porous Materials. *Adsorption*, **2003**, *9*, 9–16.

[27] Myers, A. L. Thermodynamics of Adsorption in Porous Materials. *AIChE J.*, **2002**, *48*, 145–160.

[28] Sircar, S.; Myers, A. L. Surface Potential Theory of Multilayer Adsorption from Gas Mixtures. *Chem. Eng. Sci.*, **1973**, *28*, 489–499.

[29] Callen, H. B. *Thermodynamics and an Introduction to Thermostatistics*, Wiley: New York 1985.

[30] Myers, A. L.; Monson, P. A. Adsorption in Porous Materials at High Pressure:? Theory and Experiment. *Langmuir*, **2002**, *18*, 10261–10273.

[31] Weng, C.-I.; Ju, S.-P.; Fang, K.-C.; Chang, F.-P. Atomistic Study of the Influences of Size, VDW Distance and Arrangement of Carbon Nanotubes on Hydrogen Storage. *Computational Materials Science*, **2007**, *40*, 300–308.

[32] Han, S. S.; Furukawa, H.; Yaghi, O. M.; Goddard III, W. A. Covalen Organic Frameworks as Exceptional Hydrogen Storage Materials. *J. Am. Chem. Soc.*, **2008**, *130*, 11580–11581.

[33] Furukawa, H.; Yaghi, O.M. Storage of Hydrogen, Methane, and Carbon Dioxide in Highly porous Covalent Organic Frameworks for Clean Enery Applications. *J. Am. Chem. Soc.*, **2009**, *131*, 8875–8883.

[34] Li, Y.; Yang, R. T. Hydrogen Storage in Metal-Organic and Covalent-Organic Frameworks by Spillover. *AIChE J.*, **2008**, *54*, 269–279.

[35] Hohenberg, P.; Kohn, W. Inhomogeneous Electron Gas. *Phys. Rev.*, **1964**, *136*, B864–B871.

[36] Kohn, W.; Sham, L. J. Self-Consistent Equations Including Exchange and Correlation Effects. *Phys. Rev.*, **1965**, *140*, A1133–A1138.

[37] Fulde, P. *Electron Correlations in Molecules and Solids*, Springer: Verlag Berlin Heidelberg 1995.

[38] Kristyan, S.; Pulay. Can (Semi)Local Density Functional Theory Account for the London Dispersion Forces? *Chem. Phys. Lett.*, **1994**, *229*, 175–180.

[39] Silbey, R. J.; Alberty, R. A.; Bawendi, M. G. *Physical Chemistry*, Wiley: New York, 2005; pp 371–377.

[40] Magnasco, V. *Methods of Molecular Quantum Mechanics*, Wiley: Chichester, 2009; pp 135–136.

[41] Cao, D.; Lan, J.; Wang, W.; Smit, B. Lithium-Doped 3D Covalent Organic Frameworks: High-Capacity Hydrogen Storage Materials. *Angew. Chem. Int Ed.*, **2009**, *48*, 4730–4733.

[42] Lochan, R. C.; Head-Gordon, M. Computation Studies of Molecular Hydrogen Bind Affinities: The role of Dispersion Forces, Electrostatics, and Orbital Interactions. *Phy. Chem. Chem. Phy.*, **2006**, *8*, 1357–1370.

[43] Klontzas, E.; Tylianakis, E.; Froudakis, G. E. Hydrogen Storage in 3D Covalent Organic Frameworks. A multiscale Theorectical Investigation. *J. Phys. Chem. C*, **2008**, *112*, 9095–9098.

[44] Wang, F.G.; Landau, D.P. Efficient, Multiple-Range Random Walk Algorithm to Calculate the Density of States. *Phys. Rev. Lett.*, **2001**, *86*, 2050–2053.

[45] Wang, F.G.; Landau, D.P. Determining the Density of States for Classical Statistical Models: A Random Walk Algorithm to Produce a Flat Histogram. *Phys. Rev. E*, **2001**, *64*, 056101.

[46] Desgranges, C.; Delhommelle, J. Evaluation of the Grang-Canonical Partition Function Using Expanded Wang-Landau Simulations. I. Thermodynamic Properties in the Bulk and at the Liquid-Vapor Phase Boundary. *J. Chem. Phys.* **2012**, *136*, 184107.

[47] Desgranges, C.; Delhommelle, J. Evaluation of the Grand-Canonical Partition Function Using Expanded Wang-Landau Simulations. II. Adsorption of Atomic and Molecular Fluids in a Porous Material. *J. Chem. Phys.* **2012**, *136*, 184108.

[48] Reichl, L. E. *A Modern Course in Statistical Physics*, University of Texas Press: Austin,1980; pp 246–248.

[49] Lan, J.; Cao, D.; Wang, W. Li-Doped and Nondoped Covalent Organic Borosilicate Framework for Hydrogen Storage. *J. Phys. Chem. C*, **2010**, *114*, 3108–3114.

[50] Mendoza-Cortes, J. L.; Goddard III, W. A.; Furukawa, H.; Yagi, O.M. A Covalent Organic Framework that Exceeds the DOE 2015 Volumetric Target for H2 Uptake at 298 K. *J. Phys. Chem. Lett.*, **2012**, *3*, 2671–2675.

[51] Koenig, A.R.V.; Desgranges, C.; Delhommelle, J. Adsorption of Hydrogen in Covalent Organic Frameworks Using Expanded Wang-Landau Simulations. *J. Mol. Sim.,* **2014**, *40*, 71–79.

[52] Vargaftik, N. B.; Vinoradov, Y. K.; Yargin, V. S. *Handbook of Physical Properties of Liquids and Gases*, Begell House: New York, 1996.

[53] Han, S. S.; Goddard III, W. A. Lithium-Doped Metal-Organic Frameworks for Reversible H2 Storage at Ambient Temperature. *J. Am. Chem. Soc.*, **2007**, *129*, 8422–8423.

[54] Mendoza-Cortes, J. L.; Han, S. S.; Goddard III, W. A. High H2 Uptake in Li-, Na-, K-Metalated Covalent Organic Frameworks and Metal Organic Frameworks at 298 K. *J. Phys. Chem. A*, **2012**, *116*, 1621–1631.

[55] Wu, M. M.; Wang, Q; Sun, Q.; Jena, P.; Kawazoe, Y. First-Principles Study of Hydrogen Adsorption in Metal-Doped COF-10. *J. Chem. Phys.*, **2010**, *133*, 154706.

[56] Choi, Y. J.; Lee, J. W.; Choi, J. H.; Kang, J. K. Ideal Metal-Decorated Three Dimensional Covalent Organic Frameworks for Reversible Hydrogen Storage. *Appl. Phys. Lett.*, **2008**, *92*, 173102.

[57] Yaghi, O. M. U.S. Department of Energy Hydrogen and Fuel Cells Program 2011 Annual Progress Report. Hydrogen Storage.
http://www.hydrogen.energy.gov/pdfs/progress11/iv_c_2_yaghi_2011.pdf

[58] Berendsen, H. J. C.; Postma, J. P. M.; DiNola, A.; Haak, J. R. Molecular Dynamics with Coupling to an External Bath *J. Chem. Phys.* **1984**, *81*, 3684–3690.

[59] Bussi, G.; Donadio, D.; Parrinello, M. Canonical Sampling Through Velocity Rescaling. *J. Chem. Phys.* **2007**, *126*, 014101.

[60] Parrinello, M.; Rahman, A. Polymorphic Transitions in Single Crystals: A New Molecular Dynamics Method. *J. Appl. Phys.*, **1981**, *52*, 7182–7190.

[61] de Groot, B. L. Max Planck Institute for Biophysical Chemistry.
http://www3.mpibpc.mpg.de/groups/de_groot/compbio1/p1/index.html

[62] Jorgensen, W.L.; Maxwell D.S.; Tirado-Rives, J. Development and Testing of the OPLS All-Atom Force Field on Conformational Energetics and Properties of Organic Liquids. *J. Am. Chem. Soc.*, **1996**, *118*, 11225–11236.

[63] Maruyama, S.; Kimura, T. 2000 ASME International Mechanical Engineering Congress and Exhibit. Molecular Dynamics Simulation of Hydrogen Storage in Single-walled Carbon Nanotubes.

[64] Lee, J. New Jersey Institute of Technology.
http://solar.njit.edu/~leej/lecture/ph641/ch06_summary.pdf

[65] *CRC Handbook of Chemistry and Physics.* ed. 85, p.21.

[66] Hoge, H. J.; Arnold, R.D. Vapor Pressures of Hydrogen, Deuterium, and Hydrogen Deuteride and Dew-Point Pressures of Their Mixtures. *J. Res. Natl. Bur. Stand.*, **1951**, *47*, 63–74.

[67] van Itterbeek, A.; Verbeke, O.; Theewes, F.; Staes, K.; de Boelpaep, J. The Difference in Vapour Pressure Between Normal and Equilibrium Hydrogen. Vapour Pressure of Normal Hydrogen Between 20 K and 32 K. *Physica*, **1964**, *30*, 1238–1244.

[68] Egelstaff, P.A.; Haywood, B.C.; Webb, F.J. Molecular Motions in Liquid and Solid Hydrogen and Deuterium. *Proc. Phys. Soc.*, **1967**, *90*, 681–696.

[69] Miller, T.F.; Manolopoulos, D.E. Quantum Diffusion in Liquid Para-Hydrogen from Ring-Polymer Molecular Dynamics. *J. Chem. Phys.*, **2005**, *122*, 184503.

[70] Ludwig-Bolkow-Systemtechnik GMbh. Hydrogen Data.
http://www.h2data.de